Development of a guide system for free neutron oscillation searches at the European Spallation Source

Linnéa Björk

Thesis for the degree of Master of Science in Engineering Physics

Supervisors: Mats Lindroos, Valentina Santoro & Udo Friman-Gayer
Examiner: Oxana Smirnova

Spring semester 2023

Abstract

In this project, a neutron delivery system for the study of free neutron oscillations at the HIBEAM beamline at the European Spallation Source (ESS) has been developed. The HIBEAM experiment is part of a two-stage program at ESS which will address open questions in physics; specifically the nature of dark matter and the observed asymmetry between matter and antimatter in the Universe. This will be done through high-sensitivity searches for hypothetical free neutron oscillations to antineutrons and sterile neutrons, the latter being a candidate for dark matter. These oscillation processes violate baryon number conservation and so their observation could help explain the matter-antimatter asymmetry.

The primary focus of this thesis was the development of a guide system for the search for neutron to antineutron oscillations. A few different guiding systems were tried out and optimized, with the best performing setup consisting of an elliptic guide in the so called monolith and a 20 m long second elliptic guide which was constructed as an extension of the first one. It was shown that with this optimized setup at the HIBEAM beamline, an increased sensitivity for free neutron to antineutron conversion searches compared to previous experiments can be obtained. A guide system for neutron to sterile neutron searches was also developed. Two setups were tried in this case, which consisted of a curved guide together with two different monolith guides. Both guide systems are shown to be viable options for a search for sterile neutrons in their current state, however they could also function as a base for further optimization.

Acknowledgements

First of all I want to thank Valentina Santoro, without whom this thesis would have not existed. She has always seen possibilities and gone to great lengths to accomodate my wishes ever since I wrote to her wanting to do a thesis at ESS.

During this project, I've also had the unwavering support of Udo Friman-Gayer. Without him it would have been very hard to achieve these results – he has with patience and kindness guided me through every step of the way.

A special thanks too to Mats Lindroos and Oxana Smirnova, the principal supervisor and examiner of this project.

Lastly I want to say thank you to everyone whom I have had the pleasure of working and interacting with at ESS during this project. It has been a most rewarding experience.

Abbreviations

BNV	Baryon Number Violation
EMG	Elliptic Monolith Guide
ESS	European Spallation Source
FOM	Figure Of Merit. Also called sensitivity
HIBEAM	High Intensity Baryon Extraction and Measurement
ILL	Institut Laue-Langevin
LOS	Line Of Sight
NBOA	Neutron Beam Optical Assembly
NBPI	Neutron Beam Port Insert
SM	Standard Model of particle physics
TOF	Time Of Flight
VB	Venetian Blinds

Table of Contents

1 Introduction

This project is devoted to the design of a neutron delivery system for the search for free neutron oscillations at ESS. The structure of the report is outlined in the following. First an introduction is given to ESS, together with the scientific motivation for the project. The objectives are stated. In chapter 2, the specifics of the experiments that have been studied are detailed, with theoretical background and possible experimental setup. A description of a previous free neutron oscillation experiment is given. Later in chapter 3, a background with explanations of relevant concepts is provided. The methodology is then outlined in chapter 4. The main part of the project is found in chapter 5, where the results are presented. Lastly, a summarizing discussion and outlook is given in chapter 6.

1.1 The European Spallation Source

The European Spallation Source is currently being built in Lund, Sweden and it will be the world's most powerful pulsed neutron source when it is finished. It is an international collaboration with 13 member states and many partners over the globe, with a wide range of research to be carried out once it is in operation [1]. Currently 15 instruments[1] are approved and under construction, spanning many areas of neutron science [2]. A general overview of ESS can be found in figure 1.1.

The process of how neutrons are produced at ESS will here be explained. The first step consists of accelerating protons in a 600 m long linear accelerator. The protons come from an ion source and are accelerated to 2 GeV until they hit a rotating target wheel made of tungsten. The rotation of the target wheel means subsequent beam pulses hit the target in different places, which allows it to cool and reduces radiation damage. The average power of the ESS accelerator will be 5 MW at full operation, with proton pulses 2.86 ms seconds long discharged at a frequency of 14 Hz [3]. However, the ESS accelerator will in the first stage of operation run with a power of 2 MW.

The second step is the creation of neutrons through spallation, a process where high-energy particles, such as protons, interact with atomic nuclei through inelastic nuclear reactions. Particles including protons, neutrons and alpha particles are subsequently emitted and the goal for a neutron spallation facility like ESS is to extract the emitted neutrons [4]. The neutrons first pass through a moderator, which is placed 137 mm above the target wheel [5]. The function of the moderator is to provide the experiments

[1] Instrument means the setup along the beamline in between the source and the target station, i.e. not including the target configuration as opposed to an experiment.

with neutrons of a thermal and cold spectrum of energies (see section 3.1). The neutrons are then sent towards a system of beamports, which are located in the so called monolith 2 m away from the moderator, see figure 1.2. The monolith wall is 3.5 m thick and made of stainless steel. Further out, with a radius depending on the sector, there is an additional shielding area that is called the bunker. The bunker consists mostly of heavy concrete and outside this area the radiation dose will be reduced to under 3 μSv/h in the places where staff have access [6].

The third and final step is to guide the neutrons from the beamports to the target stations of the experiments in the experimental halls. This is done by the neutron instruments, which will filter and focus neutrons emitted by the moderator to create optimal conditions for experimentation. The instruments include optics that can be placed in inserts in the monolith beamports, and optics located outside the monolith wall. The optics setup placed in the monolith, the so called monolith guide, cannot easily be removed or changed because of the high radiation dose it will be exposed to. This means that the design of this component will be exceptionally important.

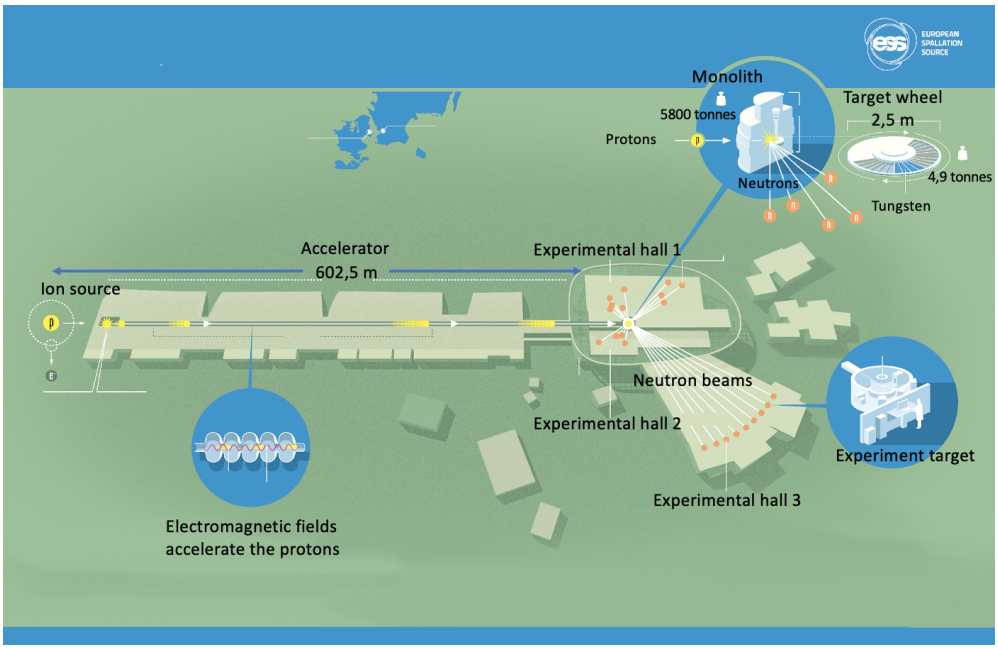

Figure 1.1: Overview of ESS. Protons are accelerated towards a tungsten target, where neutrons are created through spallation and thereafter sent to the beamports which are the start of the beamlines. The neutrons are then delivered to the experimental target stations by the different instruments. The ion source and the experimental halls are marked out, as well as the ESS target monolith. Adapted from [7].

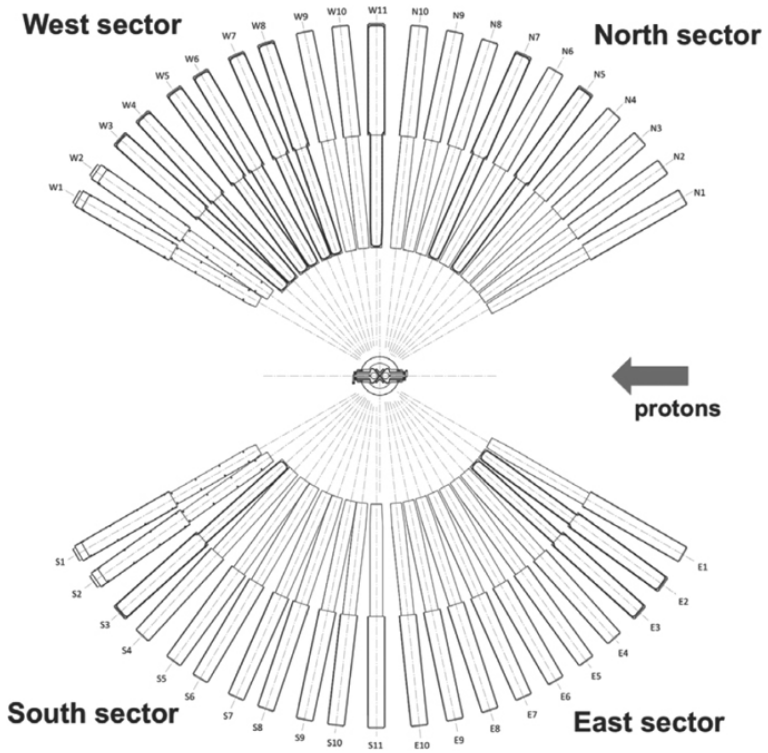

Figure 1.2: Overview of the beamports at ESS [6]. These are divided into four sectors; north, east, south and west. The beamport inserts which will be introduced here can be filled with neutron optics.

1.2 Scientific motivation

The building blocks of matter, i.e. the elementary particles, and their interactions are described by the standard model of particle physics (SM) [8]. The SM is however not complete – it leaves several questions unanswered, including the nature of dark matter and why there is more matter than antimatter in the Universe [9]. One theory for dark matter is that there exists a "mirror sector" in which all SM particles have a corresponding mirror particle [10]. These particles are often called sterile since they do not seem to interact with known particles other than via gravity. Regarding the asymmetry between matter and antimatter, there is a set of conditions that could explain this discrepancy called the Sakharov conditions [11]. One of them is the non-conservation of baryon number. Baryon number is a quantum number which for baryons, like neutrons, is +1 and for antibaryons such as antineutrons -1 [12]. According to the SM, baryon number should be conserved, meaning that the sum of baryon numbers for all particles involved in an interaction is the same before and after. If however there are processes that do not conserve this property, it could explain the observed abundance of matter over antimatter in the Universe – otherwise there would be equal amounts of each. Baryon number violation (BNV) has not yet been observed but some examples of hypothetical BNV-processes are neutron oscillations, which include neutron to sterile neutron oscillations and neutron to antineutron oscillations [6]. The sterile neutron

would be a dark matter particle from this mirror sector while the antineutron is the antiparticle of the neutron; having the same mass as the neutron but opposite signs of all charges [11].

The aim of the HIBEAM/NNBAR program at ESS is to seek answers to the dark matter and matter-antimatter problems by studying free neutron oscillations. The neutrons are free in the sense that they are not bound in an atomic nucleus and do not interact with any other particles. The High Intensity Baryon Extraction and Measurement (HIBEAM) experiment will primarily search for hypothetical sterile neutrons, as a candidate for dark matter. NNBAR will look for neutron to antineutron conversions; the experiment name comes from the fact that antineutrons are written $\bar{n}$, which is read as "n-bar". The program is divided in two stages; first studies will be carried out at the HIBEAM beamline, which is a standard beamline at ESS, and later a larger beamline for NNBAR will be installed (more details in section 2). Although the main goal of the HIBEAM experiment is looking for sterile neutrons, it could also be used to search for oscillations between neutrons and antineutrons, as a scaled-down version of the NNBAR experiment.[6]

Observations of neutron transitions to sterile neutrons and antineutrons can not only help in understanding dark matter and the matter-antimatter asymmetry; they can also reveal information about neutrino mass generation and other extensions of the standard model [6]. The discovery of such a neutron oscillation would mean an immense breakthrough in particle physics and it is therefore an exciting field to explore. So far, neutron oscillation processes have not been the subject of extensive studies, but the unprecedented neutron brightness at ESS will give the facility an edge in the search for this kind of new physics [6].

1.3 Objectives

The primary focus of this thesis is neutron to antineutron oscillations, with the main objective being designing a complete neutron delivery system for neutron to antineutron searches at the HIBEAM beamline. As a second objective, a guide system for the search for neutron to sterile neutron conversions at HIBEAM has been developed. A comparison between the different monolith guides used for the two types of experiments has then be made.

2 The HIBEAM/NNBAR program

As mentioned in section 1.2, the HIBEAM/NNBAR program is comprised of two stages to search for free neutron oscillations to antineutrons and sterile neutrons. In figure 2.1, the experimental halls of ESS are shown together with the proposed locations for HIBEAM and NNBAR.

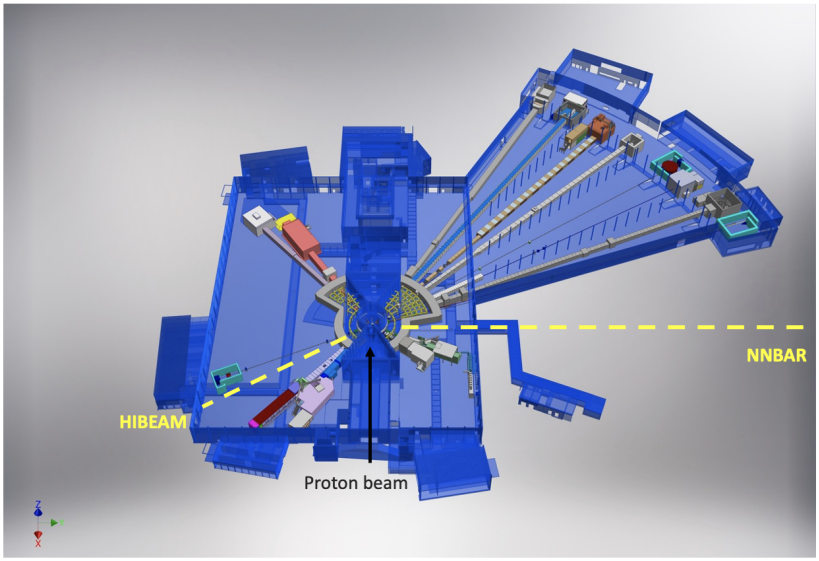

Figure 2.1: Overview of the target- and experimental halls. The proposed sites for HIBEAM and NNBAR are marked out in yellow. Adapted from [6].

The HIBEAM experiment will be located in the east sector, at beamline E6; see also figure 1.2. In figure 2.2 is seen an overview of the E6 beamline.

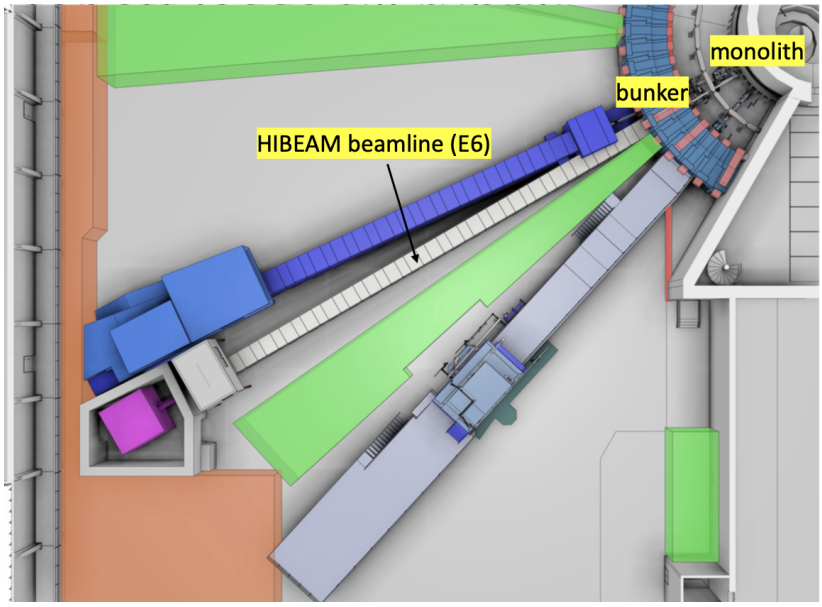

Figure 2.2: Zoomed in view of the east sector with the proposed beamline for HIBEAM, in gray, marked out [13]. The monolith wall and the bunker are shown, as well as the detector area and the length of the instrument where optics can be placed.

NNBAR will require a longer beamline; the longest proposed at ESS. It will also make use of a dedicated moderator, which will provide the experiment with higher neutron intensity and a neutron spectrum shifted to longer wavelengths [14]. It is suggested to be around 200 m long and have a so called Large Beam Port (LBP) in the monolith [15] which covers the space normally occupied by three standard ESS beamports [6]. This means there will be no beamport insert for this beamline, but a large opening which will allow for a large neutron current (defined as neutrons per second). The planned location for NNBAR is at beamports W10, W11 and N10 (cf. figure 1.2). A schematic of the NNBAR experiment can be seen in figure 2.3.

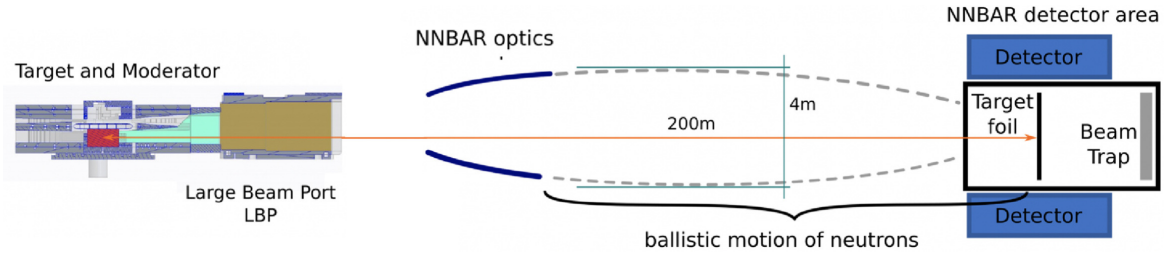

Figure 2.3: Schematic of the NNBAR experiment [16]. Neutrons are created at the target wheel to the left in the figure and pass through the moderator before traversing the LBP. Neutron optics are used to focus the neutrons onto the annihilation detector. The detector will be explained in more detail in section 3.4.

2.1 Neutron oscillations

The interesting particle in this project is the neutron which is a composite particle, a baryon, consisting of one up quark and two down quarks [17]. It has a neutral electric charge and together with protons, neutrons make up atomic nuclei. The neutron has a baryon number of +1 and a Dirac mass term which conserves baryon number. Since the SM is not complete, neutron oscillations to hypothetical sterile neutrons and neutron oscillations to antineutrons which violate baryon number by one or two units respectively are possible through extensions of the SM [6], as discussed in section 1.2. Antineutrons will hereafter be denoted as $\bar{n}$ and sterile neutrons as n'.

2.1.1 Theoretical background

In this section will be explained the idea behind neutron oscillations, with neutron to antineutron oscillations, $n-\bar{n}$, as an example. The theory is just as valid for neutron to sterile neutron oscillations, $n-n'$, and in this case the Hamiltonian can also be further developed when taking into account magnetic fields and their relation to hypothetical mirror magnetic fields in the dark sector. More details can be found in section 3.3 in [6].

The conversion from a neutron to an antineutron can be described as the mixing of a pure neutron state and a pure antineutron state, with the mixing term $\epsilon_{n\bar{n}}$. The Hamiltonian is written as [6]

$$\mathcal{H} = \begin{pmatrix} E_n & \epsilon_{n\bar{n}} \\ \epsilon_{n\bar{n}} & E_{\bar{n}} \end{pmatrix} \tag{2.1}$$

where the energies of the neutron and antineutron E_n and $E_{\bar{n}}$ respectively are not necessarily the same. In addition, environmental effects can further shift these levels in relation to each other [6].

The probability of finding an antineutron after a time t if it is in the neutron state at $t = 0$ can be expressed as[1]

$$P_{n\bar{n}}(t) = \frac{\epsilon_{n\bar{n}}^2}{(\Delta E/2)^2 + \epsilon_{n\bar{n}}^2} \sin^2\left(t\sqrt{(\Delta E/2)^2 + \epsilon_{n\bar{n}}^2}\right) e^{-t/\tau_n} \tag{2.2}$$

where $\Delta E = E_n - E_{\bar{n}}$ and τ_n is the mean life time of a free neutron [6]. This is measured to slightly less than 15 minutes [18].

The most obvious parameter that will affect ΔE is external magnetic fields. The value of the magnetic dipole moments are the same for the neutron and the antineutron but they point in opposite directions; $\vec{\mu}_n = -\vec{\mu}_{\bar{n}}$. When a magnetic field is present the magnetic moments will interact with this so that $\Delta E = 2|\vec{\mu}_n \vec{B}|$. According to equation

[1] Natural units are used in this section so $c = \hbar = 1$.

(2.2), the probability to find an antineutron is decreased when $\Delta E \neq 0$. This means that a non-zero magnetic field will suppress the conversion probability; stressing the importance of having proper magnetic shielding when performing this experiment. To have the best possible conditions to observe neutron to antineutron oscillations, it is crucial to stay in the so called quasi-free regime, where $|\Delta E|t \ll 1$. This can be obtained in vacuum with a magnetic field close to zero. During these circumstances, equation (2.2) can be approximated as [6]

$$P_{n\bar{n}}(t) = \epsilon_{n\bar{n}}^2 t^2 = \frac{t^2}{\tau_{n\bar{n}}^2} \tag{2.3}$$

where $\tau_{n\bar{n}} = 1/\epsilon_{n\bar{n}}$ is defined as the characteristic oscillation time.

The vacuum is also crucial to have free, non-interacting neutrons. Furthermore, if an oscillation event would take place and the experiment was not carried out in vacuum the antineutron would instantly annihilate with the air molecules present, meaning the event would not be registered by the detector.

2.1.2 Antineutron searches

The concept of searching for neutron to antineutron conversions with (free) beam neutrons is illustrated in figure 2.4. Neutrons are emitted from a source and travel uninterruptedly to an annihilation detector where, if the conversion process has taken place, one will be able to measure a characteristic signal of ca 1.9 GeV (see section 3.4). The fact that the annihilation signal is so energetic and easily recognizable means that the neutron to antineutron search will not be disturbed by the large background of neutrons at the ESS to any considerable extent.

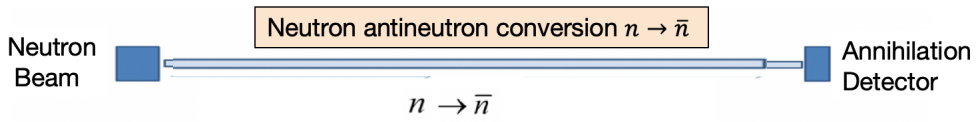

Figure 2.4: Process for detecting a neutron to antineutron oscillation event. Adapted from [6].

The performance of the optics designed in this project will be evaluated according to a single value, the so called figure of merit (FOM). For $n - \bar{n}$ searches, this is the neutron current times the mean uninterrupted time of flight (TOF) squared [6]. The probability of an oscillation event is proportional to the square of the time that has passed according to equation (2.3), and it is important that this is the uninterrupted flight time. Since neutrons and antineutrons interact differently with matter, such as the guide material, each time this happens the oscillation will be suppressed, implying that the oscillation time is reset [6]. Otherwise it is intuitive that more neutrons will increase the chance of observing an oscillation event.

The FOM can be expressed as

$$\text{FOM} = N \cdot \langle t^2 \rangle \tag{2.4}$$

where N is the number of neutrons per unit time that hit the annihilation target after an average uninterrupted flight time squared of t^2 [16]. The unit is neutrons times seconds.

2.1.3 Previous studies of $n - \bar{n}$ oscillations

The most recent experiment which studied free neutron to antineutron oscillations was performed at the Institut Laue-Langevin (ILL) in 1990 [19]. Studies of $n - \bar{n}$ oscillations for bound neutrons have been studied more recently for example at Super-Kamiokande [20]. Since the HIBEAM/NNBAR program uses free neutrons and will build on the ILL experiment, this is explained in more detail here.

The setup used at ILL can be seen in figure 2.5. Neutrons are emitted from the 58 MW high flux reactor (HFR) at ILL and are sent through a bent guide in order to filter out the fastest neutrons and reduce the background. The remaining neutrons then enter a 33.6 m long diverging neutron guide with the task to focus the neutrons onto the 1.1 m diameter annihilation target. The optics are placed inside a 95 m long vacuum tube which covers the neutrons' path from the start of the reflector to the beam dump. The oscillation region, 81 m long, was covered with magnetic shielding so that the residual magnetic field was less than 10 nT to satisfy the quasi-free condition (see section 2.1.1). 81 m was then the maximum available flight path for the neutrons; if they were not reflected in the guide they would fly this distance without interruptions.

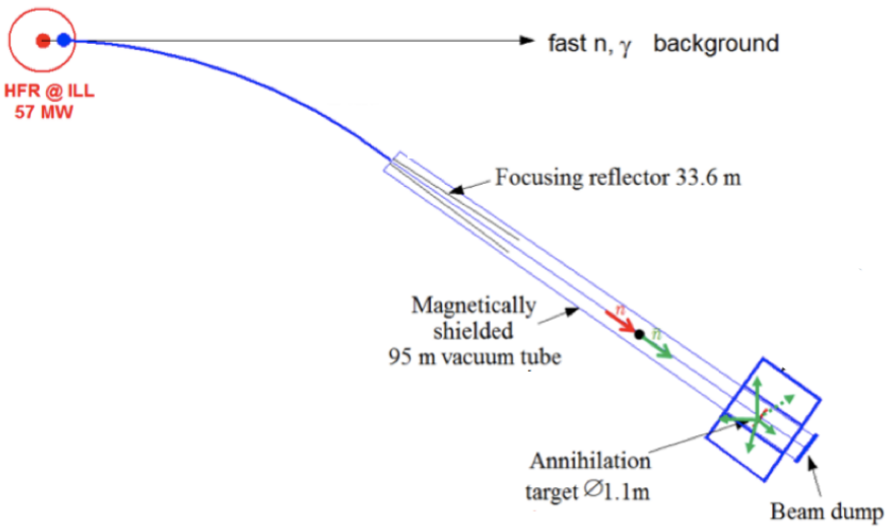

Figure 2.5: Schematic of the ILL experiment [13]. Neutrons are emitted and sent through a bent guide to filter out the fast neutrons. The neutrons later enter a reflector which focuses them onto the annihilation target.

The experiment provided a lower limit for the $n-\bar{n}$ oscillation time of $\tau_{n\bar{n}} \geq 0.86 \cdot 10^8$, since no antineutron was observed in the $2.4 \cdot 10^7$ s running time. Key experimental parameters of the ILL experiment are listed in table 2.1.

Table 2.1: Parameters of the 1994 ILL experiment [19]. Neutron current and average wavelength are measured at the target.

Max. available flight path [m]	Target diameter [m]	Neutron current [n/s]	Avg. free TOF [s]	Avg. wavelength [Å]
81	1.1	$(1.25 \pm 0.06) \cdot 10^{11}$	0.109 ± 0.002	5.9

The ILL figure of merit is $1.5 \cdot 10^9$ n·s for one year of operation, according to equation 2.4. However, one operational year at ESS will be less efficient than at ILL – this is based on operational experience from the Spallation Neutron Source (SNS) in Oak Ridge since the beam operating hours at ESS will be similar to SNS [21]. To have a more realistic comparison, 1 ILL unit will be taken as $2 \cdot 10^9$ n·s.

The setup at ESS will be similar to the one at ILL, also with magnetic shielding, vacuum tube and a neutron reflector. The NNBAR experiment will however have a much higher neutron current and more than twice as long maximum flight path. With these improvements in mind, the hope is to have an increased sensitivity, e.g. figure of merit, of three orders of magnitude for NNBAR compared to the ILL when the ESS accelerator is running at full operation of an average of 5 MW [6].

2.1.4 Sterile neutron searches

Principles to search for sterile neutrons include "bottle" and "beam" experiments [6]. The first involves storing ultra-cold neutrons (UCNs) in a material or magnetic trap and counting the number of neutrons left at different times. This is a way to measure the neutron lifetime, but if some of the neutrons were to decay to sterile neutrons, they could escape from the bottle and one would possibly be able to measure a lower value for the neutron lifetime than the one predicted by the standard model [6, 22]. The bottle experiment is shown in figure 2.6.

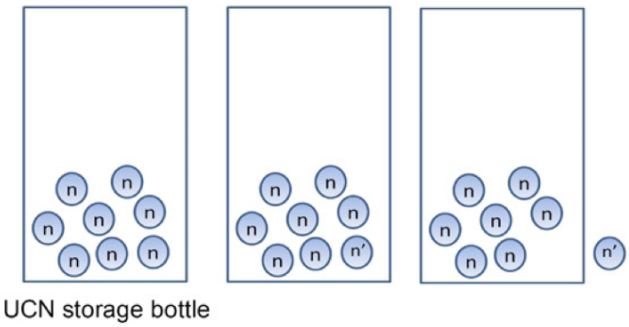

Figure 2.6: UCN bottle experiment [6]. After some time, neutrons could convert to sterile neutrons and these would then be able to "escape" from the bottle.

The experiments with beam neutrons are outlined in the following and they are illustrated in figure 2.7. These searches have not been performed before, but development on how to experimentally implement this at HIBEAM is ongoing [6].

1. Disappearance: neutrons are converted to sterile neutrons when allowed to fly freely for an amount of time. A measured decrease of the neutron flux at the detector would testify that neutrons have oscillated to sterile neutrons, since these would not interact with the detector material.

2. Regeneration of neutrons: a beamstop is inserted which is designed to absorb neutrons. Neutrons could oscillate to sterile neutrons before hitting the beamstop, and the sterile neutrons would pass through. After the beamstop the sterile neutrons could be converted back to neutrons. Ideally the beamstop absorbs all incident neutrons, so if neutrons are detected at the target some oscillation process has taken place.

3. Neutron to antineutron via sterile neutron: similar to the previous case, but after the beamstop the sterile neutrons would be converted to antineutrons, requiring an annihilation detector.

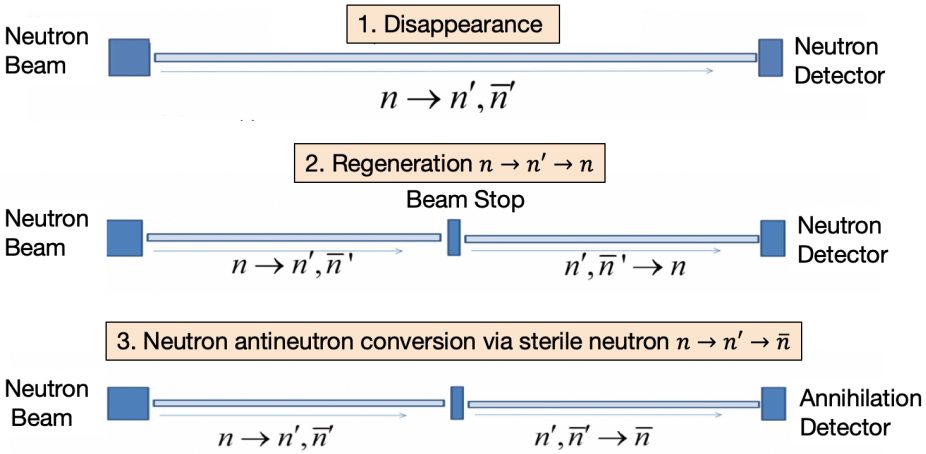

Figure 2.7: Different methods to search for sterile neutrons. The oscillation processes are however not limited to n' and $\bar{n}$; also sterile antineutrons $\bar{n}'$ could hypothetically be an oscillation product [6]. Adapted from [6].

As for antineutron searches, magnetic shielding is important when studying sterile neutron oscillations. Here one also needs to account for hypothetical mirror magnetic fields, since the oscillation probability is suppressed if these are not approximately the same as the "normal" magnetic fields. The magnitudes of such mirror magnetic fields are not known, so it will be important to scan the applied magnetic field when performing the searches in figure 2.7 to increase the oscillation probability. See also sections 3.3 and 7 in [6].

In the experiment to search for sterile neutrons at HIBEAM, the neutron background at ESS is more of an issue than in the case of antineutron searches, since here there is no characteristic high-energy peak to look for. At least in the first two modes in figure 2.7 the detectors are counting individual neutrons, so any superfluous neutrons that hit the target will make it harder to identify an oscillation occurrence. These are typically the fast neutrons, which have a shorter time of flight and so a lower oscillation probability (cf. equation (2.4)). At the same time, with more neutrons the probability to observe an oscillation event increases. For this reason, it will be important to suppress the fast neutron background but retain slow neutrons with a longer flight time and a higher oscillation probability. By losing line of sight (LOS) of the moderator the fast neutrons can be filtered out. This can for example be done with a curved guide after the monolith, which was the case in this project.

The figure of merit for $n - n'$ searches is approximated to the neutron current at the exit of the curved guide.

3 Background

3.1 Cold and thermal neutrons

Neutrons are often classified according to their energies. A rough division can be found in table 3.1.

Table 3.1: Energy ranges for different (free) neutrons [23].

Name	Energy interval [eV]
Cold neutrons	$(0 - 0.025)$
Thermal neutrons	$(0.025 - 1)$
Resonance neutrons	$(1 - 10^3)$
Fast neutrons	$(10^3 - 10^7)$

Thermal neutrons are so called because they have an energy which corresponds roughly to room temperature; their energy is ca 25 meV [23]. The neutron energy is related to wavelength and velocity through de Broglie's relation and the classical expressions for kinetic energy and momentum in equations (3.1) and (3.2), since the relevant energies are not relativistic.

$$\lambda = \frac{h}{p} = \frac{h}{mv} \tag{3.1}$$

$$E = \frac{1}{2}mv^2 \tag{3.2}$$

where $m = 1.67492749804(95) \cdot 10^{-27}$ kg is the neutron mass [18]. At ESS, the moderator will provide the experiments with thermal and cold neutrons [5], as previously stated. According to equations (3.1) and (3.2), thermal neutrons have a wavelength of ca 2 Å and a velocity of ca 2000 m/s.

3.2 Neutron optics

Neutron optics studies how a beam of free, low energy neutrons interact with matter. Neutrons, much like electromagnetic radiation, can be scattered, diffracted and reflected [24]. In figure 3.1 is seen how these low energy neutrons can be scattered in a material following Snell's law.

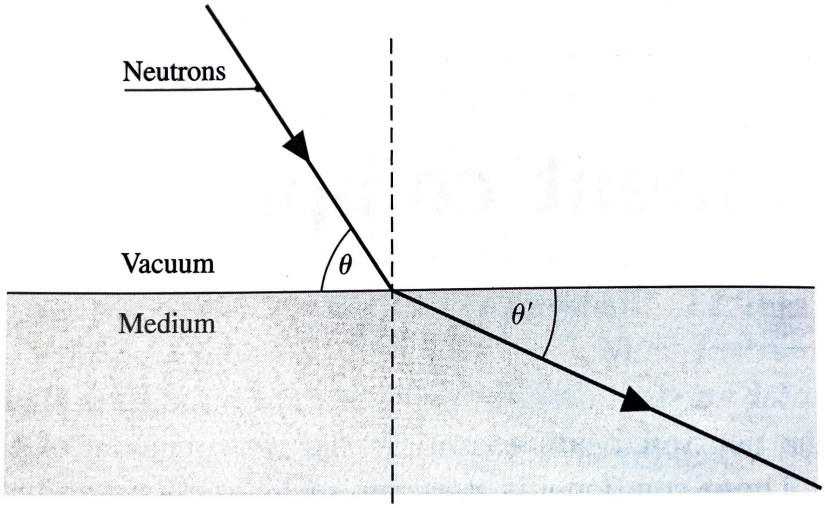

Figure 3.1: Neutrons with an incident angle θ are scattered with a glancing angle θ' [4].

The refractive indices for neutrons are for most materials less than 1, which means that total external reflection can take place in the material at its boundary with a vacuum. When θ in figure 3.1 is so small that $\theta' = 0$, the incident angle corresponds to the critical angle for total reflection, θ_c [4].

3.2.1 Neutron guides

Neutron guides can be compared to optical fibers for light, in the sense that they are both based on critical-angle scattering and provide efficient transport of their respective particles. A neutron guide typically has a rectangular cross section with smooth walls. The shape of the guide can vary depending on which function it should have. For focusing purposes, elliptic or parabolic shapes can be used, but also straight or tapered guides can be employed. If neutrons enter the guide at an angle smaller than the critical angle they will be totally reflected and continue through the guide. If they on the other hand have an incoming angle larger than θ_c they will be transmitted in the mirror material and be lost. Therefore, it is desirable to use a mirror material with a large critical angle, to minimize the neutron losses. A good choice for this is nickel.[25]

The critical angle has a wavelength dependence; θ_c increases with longer wavelength. This implies that neutrons with longer wavelength have a higher probability of being reflected in the guide while short wavelength neutrons will be lost to a greater extent. This will then mean that the wavelength distribution of neutrons at the end of the guide has been shifted towards higher values relative to how it was at the entrance.[25]

Neutron supermirrors

In recent years, progress has been made in the development of neutron guides thanks to the use of supermirrors. Such neutron supermirrors will be used for the HIBEAM and NNBAR instruments [26]. Neutron supermirrors are multilayered surfaces with differing thickness of the layers, see figure 3.2 [4]. Particularly favourable are alternating layers of nickel and titanium, since these have strongly different scattering properties. By gradually increasing the layer thickness, the supermirror can reflect beams with incident angles several times larger than the critical angle for a simple mirror [4].

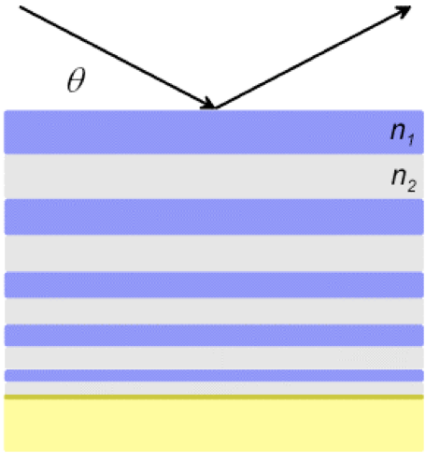

Figure 3.2: Schematic of a neutron supermirror [27]. The layer thickness decreases with depth.

The supermirror acts like a diffraction grating, where Bragg reflection occurs at different depths for different angles. Long wavelength neutrons are reflected close to the surface, where the layers are thicker, while short wavelength neutrons are transmitted through the upper layers and reflected from the ones further down in the structure. The effect of this is that a pattern of overlapping Bragg peaks will be obtained, meaning a continuous distribution of wavelengths will be reflected. The supermirror will in this way reflect a broader spectrum of wavelengths than a simple mirror, and also allow for larger angles in general. This is shown in figure 3.3, where the reflectivity is plotted as a function of wavevector transfer Q. The reflection drops when the neutron wavelength is too short to be reflected by the thinnest layer at the bottom.[25]

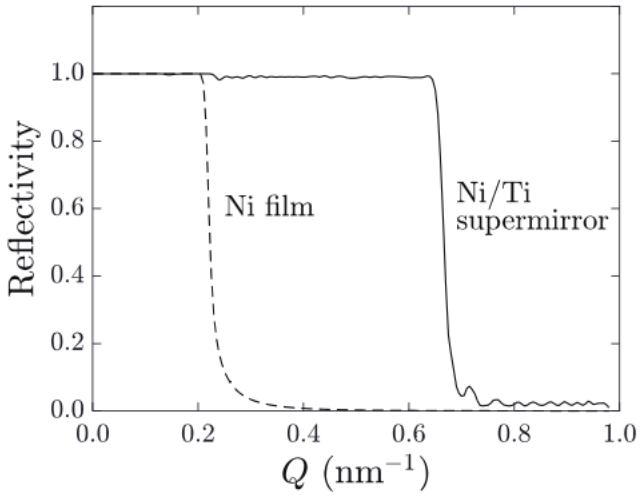

Figure 3.3: Reflectivity as a function of wavevector transfer for a Ni/Ti supermirror [25]. The reflecitivity for a simple Ni mirror is shown in dashed for comparison.

A supermirror is often characterized by its so called m-value. This is the ratio between the critical wavevector transfer Q_c for the supermirror and for nickel, where Q_c is the Q-value at the critical angle for total reflection. The relation between reflectivity, m-value and Q is displayed in figure 3.4. The decreasing slope of the reflectivity is owing to the attenuation of neutrons as the depth is increased [25].

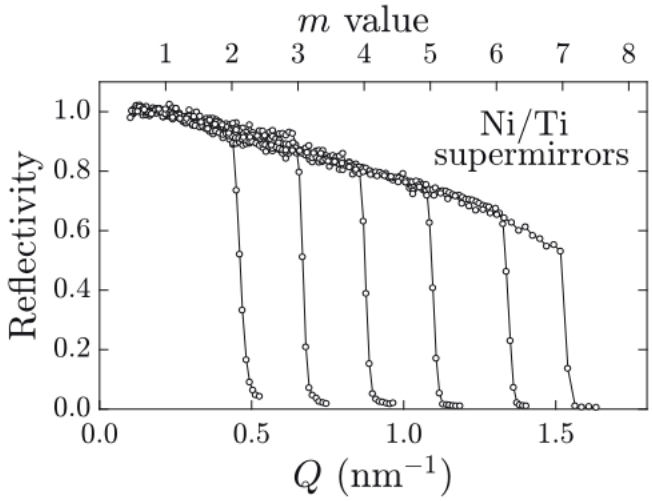

Figure 3.4: Reflectivity plot for increasing Q and m for m-values up to 7 [25].

3.2.2 Elliptic guides

The elliptic guide is the primary focusing optics piece that has been used during the course of this project. An ellipse is shaped such that a beam emitted from one of its

focal points will be reflected to the other focal point [26], see figure 3.5. Ellipses are characterized by their focal length f and their semi-axes a and b. The longest line that can be drawn between two points on the ellipse surface, going through the focal points and the center, is called the major axis. The longest line that can be drawn perpendicular to this one is the minor axis. a and b are then called the semi-major axis and semi-minor axis respectively, since they represent half the width and height of the ellipse.

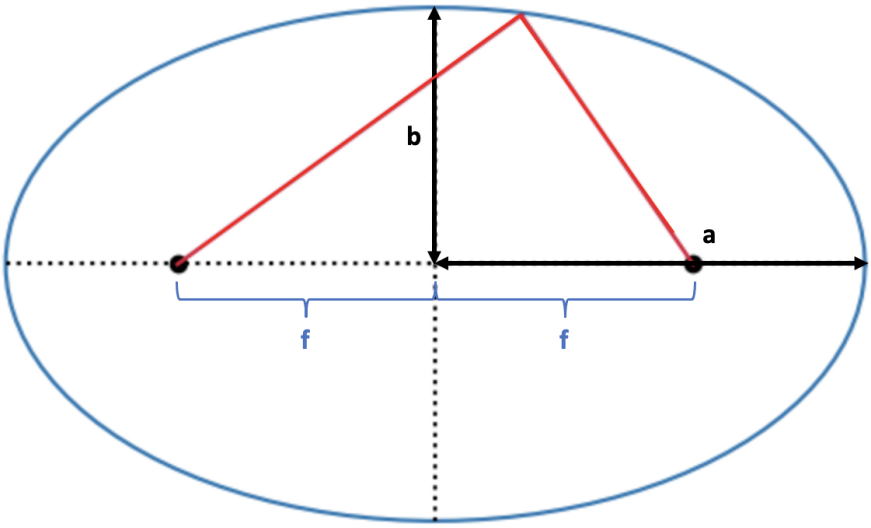

Figure 3.5: Ellipse. The focal points are marked out as black dots, placed at the focal distance f from the origin. The red line represents a beam originating from one focal point and being reflected to the other. The semi-axes a and b are marked out in black.

The equation of an ellipse with width $2a$ and height $2b$ which is centered at the origin is given by

$$\frac{x^2}{a^2} + \frac{y^2}{b^2} = 1. \tag{3.3}$$

The relation between the semi-axes and the focal length is

$$f = \sqrt{a^2 - b^2} \tag{3.4}$$

with the focal points located at $(\pm f, 0)$.

3.2.3 Nested mirrors

There exist an infinite number of possible ellipses for a set of focal points. This can be used to construct a nested optics system, with short guides of reflector material

stacked on top of each other to create a layered component. This is shown in figure 3.6.

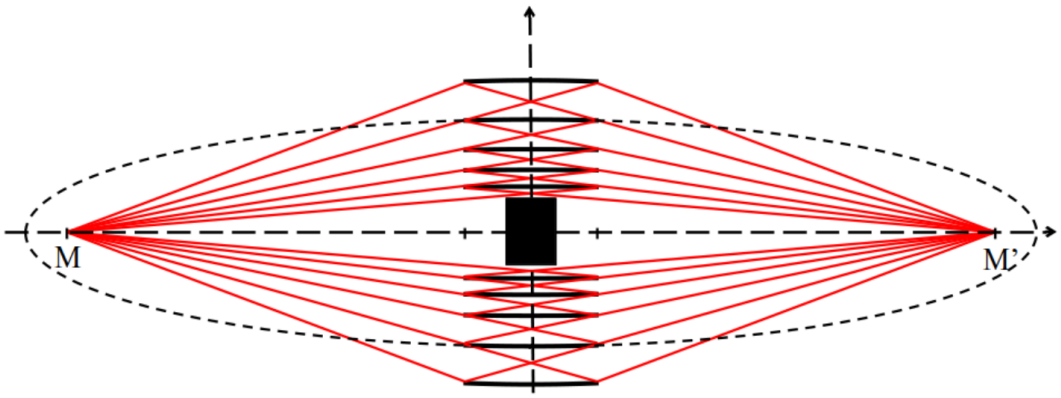

Figure 3.6: Nested mirror system [26]. The layers, in solid black, are parts of ellipses with the focal points M and M'. The dashed outline shows one of the ellipses. The black rectangle represents an absorber which blocks the direct view of the source [28].

Looking at figure 3.6, the nested mirror can be thought of as a set of ellipses from which a certain range has been cut out and where the parts have then been placed on top of each other. It works the same way as an ellipse; focusing a beam originating in one focal point to the other focal point. The absorber used in this example is however not a necessary part of the component; the nested mirror system can look slightly different for different purposes.

The field of nested mirror optics has much potential but so far only small scale nested mirror systems for neutrons have been realized; see for example [29]. Some advantages of a nested mirror system compared to an elliptic guide include flexible positioning and compactness of the component, which has the potential to increase the average TOF for the neutrons. Drawbacks include loss of neutrons in the blade material since the blades have a finite thickness and mechanical complications regarding construction of a suitable holding structure as well as gravitational bending of the blades [29].

3.3 Moderator

The ESS moderator has a shape resembling a butterfly, from whence its name "the butterfly moderator" was derived. See figure 3.7. The moderator is relatively flat; only 3 cm high. This is because one wants to mitigate the number of neutrons that are absorbed in the moderator material – they should be slowed down but not stopped [5].

The goal of the moderator is to provide bispectral beams for the instruments, meaning

it will be a source of both thermal and cold neutrons. How this will work is conceptually illustrated in figure 3.8. To achieve this, the moderator is composed of two parts; the cold moderator with parahydrogen as active material and the thermal moderators with water [5]. In figure 3.7 the dark blue area is the cold moderator, while the cross shaped lighter blue parts in between are the thermal moderators.

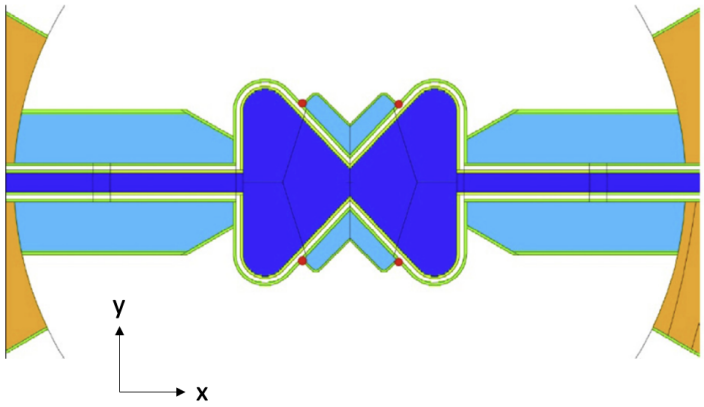

Figure 3.7: The ESS butterfly moderator [5]. The red points in the figure are the focal points which the beamlines will be facing to extract neutrons. The dark blue butterfly shape is the cold moderator, the light blue cross shapes are the thermal moderators.

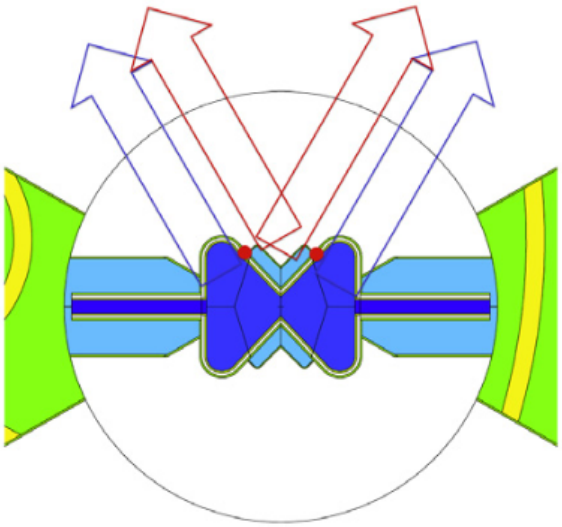

Figure 3.8: Extraction configurations for thermal (red arrows) and cold (blue arrows) neutrons [5].

3.4 Detector

The detector choice depends on which experiment one wants to investigate; $n - \bar{n}$ searches or $n - n'$ searches, and then which of the three methods for neutron to sterile neutron searches to be employed (see sections 2.1.2 and 2.1.4). Since the main topic of this thesis is neutron to antineutron oscillations, the concept of an annihilation detector such as will be used for NNBAR will here briefly be explained.

The target, where the antineutron annihilation will take place, is made of carbon. Two different target sizes, based on realistic, existing detector systems, were tried out in this thesis to calculate the sensitivities on $n - \bar{n}$ searches at the HIBEAM beamline. The targets in questions had a diameter of 1 m and 0.4 m respectively. A larger target is naturally better for obtaining a higher FOM, but this will also cost more.

When an antineutron hits the target, it will interact with the nucleons in the carbon atoms and annihilation can take place. The energy release from annihilation in the antineutron-nucleon system is 1.88 GeV, a characteristic peak. The process produces pions, both π^+, π^- and π^0, with five produced pions on average for each annihilation [30]. In figure 3.9 the different decay channels for an $n - \bar{n}$ annihilation event are shown.

$n - \bar{n}$ annihilation mode	Branching Ratio
$\pi^+\pi^-3\pi^0$	28%
$2\pi^+2\pi^-\pi^0$	24%
$\pi^+\pi^-2\pi^0$	11%
$2\pi^+2\pi^-2\pi^0$	10%
$\pi^+\pi^-\omega$	10%
$2\pi^+2\pi^-$	7%
$\pi^+\pi^-\pi^0$	6.5%
$\pi^+\pi^-$	2 %
$2\pi^0$	1.5 %

Figure 3.9: Branching ratios for the final states in a neutron-antineutron annihilation. The most common channels are combinations of 5 pions. Adapted from [31].

Neutral pions have a short lifetime compared to the expected flight time inside the detector and will not have time to be detected – here one looks instead for a $\gamma\gamma$-signal which is a strong decay channel for π^0. The charged pions can be detected in the calorimeter and a large part of the energy released in the annihilation event is in the form of rest mass for these pions. By summing up their masses and the gamma ray energies one would be able to reconstruct the annihilation event. With the proposed detector design, one observed annihilation is enough to prove that this oscillation takes place. However, one must also take into consideration that the detector efficiency will not be 100%.[30]

As discussed in section 2.1.2, the neutron background at ESS will not be too much of a problem for the $n-\bar{n}$ search. The most likely background source that could produce high energy events on the same scale as the annihilation signal is cosmic rays [6]. It is therefore important that the cosmic rays can be identified and filtered out from the detector data [19]. This is done with a so called cosmic veto, whose purpose is to reject events which originate from cosmic rays [6, 30].

The cross-sectional view of a proposed annihilation detector is shown in figure 3.10.

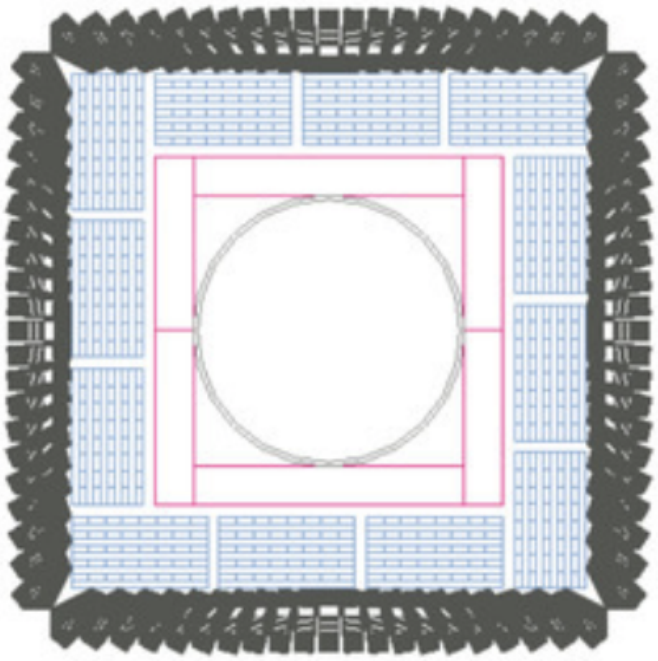

Figure 3.10: Schematic of the proposed NNBAR annihilation detector [30]. The carbon target disk is placed inside the light gray, cylindrical aluminium tube. In pink is seen the time projection chamber, outside this in light blue are scintillator modules and furthest out a calorimeter in lead glass. The cosmic veto is not marked out. For more details see [30].

4 Methodology

4.1 Software

4.1.1 McStas

In this project, the neutron ray-tracing simulation program `McStas` was used [32, 33]. `McStas` is designed to simulate neutron interactions with matter in the energy regime where neutrons can be approximated as optical rays. These can be called slow neutrons, in which both thermal and cold neutrons are included. `McStas` uses Monte Carlo methods to generate the neutron tracks, i.e. randomized inputs are generated and tried with the model to find numerical results [34]. In the project, `McStas` version 3.2 was used.

As Monte Carlo methods are subject to statistical variances, a way to reduce the impact of this is to use so called importance sampling where samples are taken more often for processes and in regions that are of higher importance for the result [32]. This has been implemented in `McStas` and one can think of it as each neutron being assigned a weight which is calculated from the probability of the neutron reaching its destination depending on factors such as cross sections, angular distributions and mean free paths. The weight will be updated during the course of the simulation according to the path of the neutron. As an example, if an optical component with a reflectivity of 20% is used in a simulation, and only reflected neutrons are of interest for the rest of the simulation, the neutron weight will be multiplied by 0.20 when being reflected in the component [34]. A simulated neutron with this adjusted weight will be denoted as a neutron track or ray in the following sections. When running a simulation in `McStas`, the number of tracks is specified.

`McStas` uses the term intensity to describe the sum of all simulated rays [32]. This can then be written as

$$I = \sum_i p_i \tag{4.1}$$

where p_i are the weight factors. The uncertainties are calculated as

$$\sigma^2(I) = \sum_i p_i^2. \tag{4.2}$$

The reader is referred to [32] and [33] for more details.

4.1.2 McStasScript and GitHub

In the project, a python API called `McStasScript` was used in order to facilitate the use of McStas [35]. `McStasScript` enables one to manipulate simulations and access the results more easily.

Development of the software used in this thesis was part of the public project `HIBEAM_McStas` [36], which is dedicated to simulation code for neutron guide systems for the HIBEAM experiment. The repository `los` [37] was also used when designing the curved guide for $n - n'$ searches.

4.2 McStas geometry

The `McStas` coordinate system places the optical axis of the studied beamline in the z-direction. In the following sections, x- and y-directions will be called horizontal and vertical directions respectively. The term top view will denote the xz-plane, and side view the yz-plane.

The proposed beamline for the HIBEAM experiment is E6, as mentioned in chapter 2. In figure 4.1 an overview of a simplified beamline model for E6 as seen in `McStas` is shown, which includes all parts relevant for slow-neutron tracking, as well as some just for visualization purposes. All visualizations of `McStas` geometries were obtained with the `McStas`-tool `mcdisplay` of the instrument-file created during the simulation.

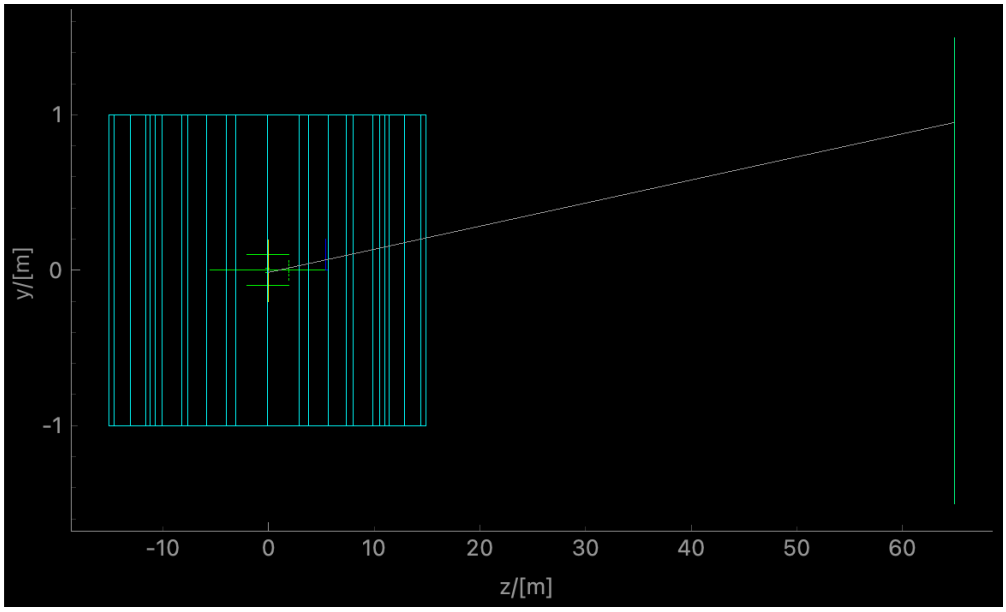

(a) Side view of the beamline.

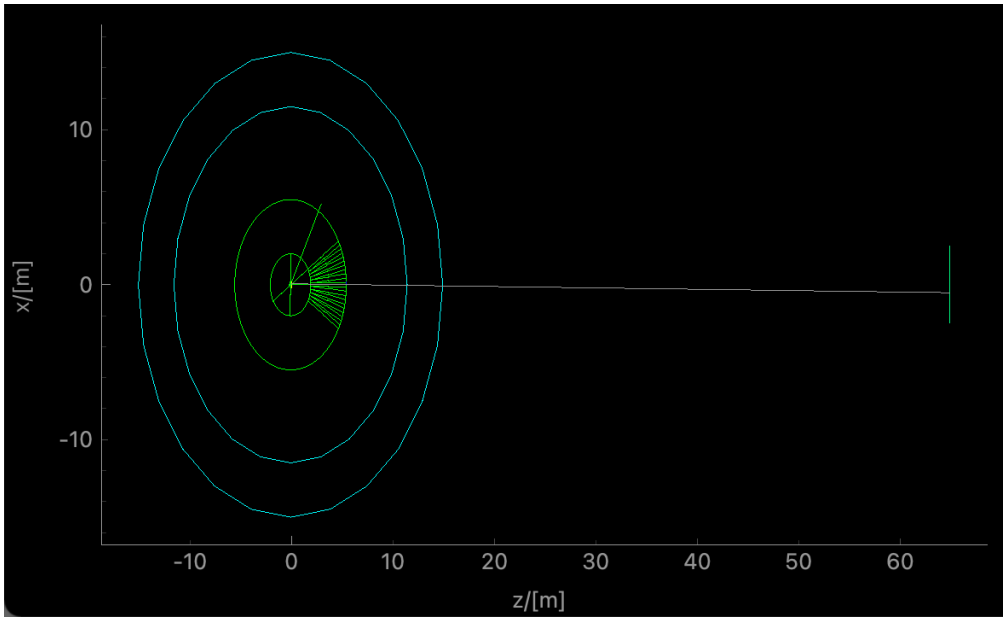

(b) Top view of the beamline.

Figure 4.1: Overview of the E6 beamline in `McStas` in side- and top view. The green circles centered at the origin in the top view show the monolith wall, with the beamport inserts marked out on the right side. The turqouise circles, also in the top view, are the walls of the bunker. The monolith and bunker walls are only for visualization. The moderator is placed at approximately $z = 0$ m. The target screen, placed 65 m away from the moderator in the z-direction, is a monitor recording all the neutrons that hit it (see section 4.4). The white streak is a neutron track that was emitted from the source and hit the target monitor.

4.2.1 Source term

The source term used in the simulations was a phenomenological model called `ESS_butterfly` [38]. In figure 4.2 the component can be seen in the top view.

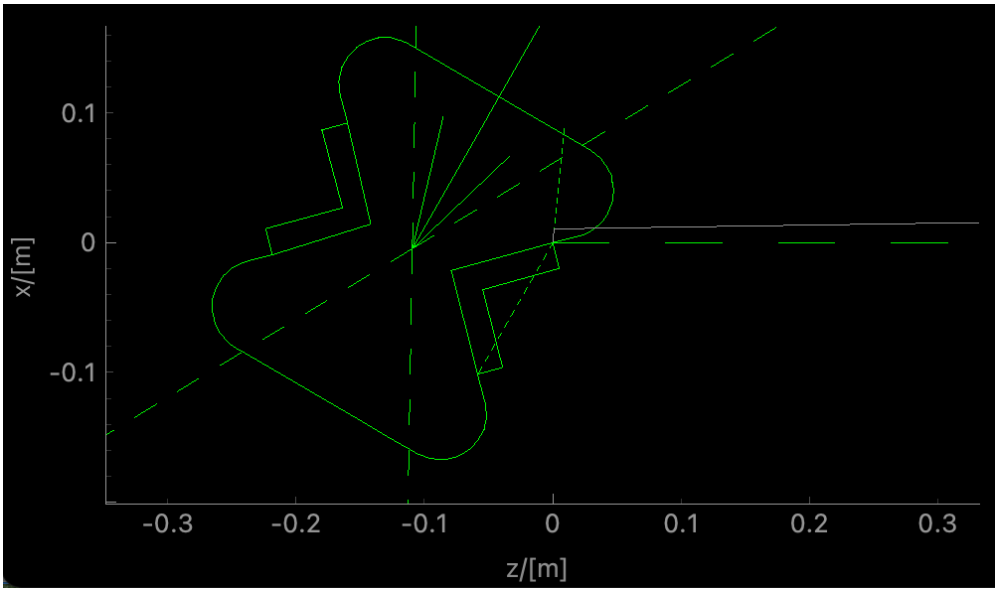

Figure 4.2: `ESS_butterfly` component in the `McStas` top view.

The shape of the moderator in figure 4.2 resembles the moderator displayed in figure 3.7. As shown in figure 4.2, the `McStas` origin is at one of the moderator's focal points and not at the center of the moderator (cf. figure 3.7). This slight shift in the z-direction had to be accounted for when placing all other components along the beamline in the `McStas` environment, since these will be placed relative to the moderator center.

Ideally, the simulations would have also been run with input created from an MCNP simulation. MCNP is a general-purpose time-dependent code designed to track particles over a wide spectrum of energies [39]. The `ESS_butterfly` model is an interpolation of MCNP simulation results that reproduces key distributions with high accuracy, but contains some approximations with respect to the correlation between phase-space variables. The model offers an increase of about a factor of 10 in the speed of a McStas simulation compared to using MCNP input, and it has been shown in other instrument studies that results produced with the `ESS_butterfly` are in reasonable agreement with fully realistic MCNP simulations. Therefore, this thesis only used the `ESS_butterfly` model as a source term. Although general optimization results, like the dimensions of the optics components, can be expected to be the same for MCNP input and the `ESS_butterfly`, a benchmark of the results of this thesis is planned in the future. This will also show whether small changes to the moderator design after 2016 (the year on which the `ESS_butterfly` model is based) have an impact.

4.3 Optics construction

In the project, some different optics pieces were used to construct the neutron guides. The McStas-components for the respective guides are listed below, the guides themselves will be explained in more detail in section 5. For all components, the time of flight is reset when a neutron track is reflected in them.

- Elliptic guide: `Guide_anyshape`, with the geometry specified in an OFF-file (see [40] for details about the .off format). The guide is approximated by a set of trapezoids put together to form a continuous shape (like a real-world instrument would be constructed).
- Nested mirror system, called Venetian blinds: The component `Venbla.com` [41].
- Tapered guide: `Guide_gravity`.
- Curved guide: Segments of `Guide_gravity` rotated and translated with respect to each other to create a segmented approximation of a continuous curve.

4.4 Recording results

$n - \bar{n}$ searches

Two ways to record the results were used in the project; with McStas monitors and with MCPL output [42]. MCPL, Monte Carlo Particle Lists, is a binary format which lists particle state information to enable interchanging particles between various Monte Carlo simulation applications [42]. The recording procedures will here be explained.

With McStas monitors, the primarily used component to record the neutron tracks was a so called `PSD_TOF_monitor` which was placed at 65 m away from the moderator in the z-direction. The monitor recorded where the tracks hit (x- and y-position), their weights and their free time of flight. The monitor had an extent of 5 m in the x-direction and 3 m in the y-direction centered around the optical axis. The 15 m^2 screen was big enough to capture practically all neutrons coming from the moderator, even without focusing optics. Since the `PSD_TOF_monitor` recorded the neutron current per space- and time bin this could be used to calculate the FOM value in the target. In the project, the values for the number of pixels and the number of time bins per pixel were fixed to

```
nx × ny = 100 × 80 = 8000
nt = 100
```

Another McStas monitor used was the `TOF_monitor`, to evaluate the average time of flight.

Regarding the MCPL output, this was introduced as the McStas component MCPL_output. This needs no dimension specification but will record, among other things, the free TOF and the weights for the neutrons that reach the location where it is placed; in this case at the target location 65 m away from the moderator.

$n - n'$ searches

PSD_monitors will be placed at the exit of the monolith guide, at the entry of the curved guide and at the exit of the curved guide. The last one is the most interesting value, since a high neutron current is desired here when most of the fast neutrons have been filtered out, but for comparative purposes monitors were also placed at the other sites of the setup. The monitors will have the same dimensions as the optics piece where they are placed. See section 5.2.3.

4.5 Analysis

The post-processing and analysis was made with Python code, using Python3.

The FOM calculation was made in two ways; either using the output data from the PSD_TOF_monitor or MCPL_output. The first was used to find the optimum target position and is an approximation of the actual FOM in equation (4.4), since it depends on the binning of the PSD_TOF_monitor. This however provided a significant computational advantage compared to looping over all the particles in the MCPL_output. The second method used equation (4.4), which is an adaptation from equation (2.4), to calculate the FOM.

- With PSD_TOF_monitor: The position and time for tracks that hit the monitor were read out. A loop over the 8000 pixels was run, where the center of a circle with a set radius r was moved over the monitor screen. For each target position (x_t, y_t), the FOM contributions by all pixels (x_i, y_i) that satifsy
$$(x_i - x_t)^2 + (y_i - y_t)^2 \leq r^2 \tag{4.3}$$
was summed. The position (x_t, y_t) which gave the highest FOM in the target was then read out, together with the FOM value and the uncertainty.
- With MCPL_output: Using the previously obtained optimum position, the FOM in target was calculated according to equation (4.4). The uninterrupted flight time t_i for a neutron with weight p_i that reached $z = 65$ m within the area specified by the condition in equation (4.3) was read out from the MCPL file, so the FOM became a sum over all neutrons in the target. The uncertainty was also calculated, inspired by equation (4.2).
$$\text{FOM} = \sum_i p_i \cdot t_i^2 \tag{4.4}$$

The binning was sufficiently fine for the `PSD_TOF_monitor` to yield values that agreed well with the FOM calculated from `MCPL`; the values obtained with the two methods were consistently within the respective error margins.

The FOM values found in this thesis were calculated with equation (4.4) from `MCPL_output` while the plots shown in the following sections were generated with the first method of calculating the FOM with respect to the optimum target position. The plots show the optimum target position as a red dot with the outline of the hypothetical target disk mapped as a red circle.

5 Neutron guide system

The main part of this thesis consisted of trying out different optics pieces and combinations of them to get optimal results for the two types of experiments at the HIBEAM beamline. In this chapter, first the study of a guide system for the search for neutron to antineutron oscillations, which was the primary focus of the thesis, will be detailed. Later, in section 5.2, a guide system to study neutron to sterile neutron conversions is presented. Lastly a comparison between the monolith guides for the different experiments will be made.

Optics can be placed in the monolith, in the so called Neutron Beam Port Inserts (NBPI), and afterwards along the whole length of the beamline, with some exceptions for components which are required by ESS, such as beam shutters. The shutters will shield the spallation target wheel when the beam is off and there is need to access the experimental area. The neutron guide used in the monolith will have a substrate made of copper with a thin layer of mirror coating and have a thickness of 8 mm on each side. The optics located outside the target monolith, hereafter called downstream optics, could however be made of cheaper material such as glass.

The NBPI places strict constraints on the monolith guide, or more properly, the Neutron Beam Optical Assembly (NBOA). The relevant constraints of the NBOA were determined in collaboration with the mechanical-engineering team at ESS. The values are shown in table 5.1, given relative to the optical axis. Here a mirror thickness of 8 mm on all sides has already been taken into account. In the horizontal direction the available space is symmetric around the optical axis. In the vertical direction the space is more strongly limited at the top than at the bottom.

Table 5.1: Engineering constraints of the NBOA. Values are given relative to the optical axis. Mirror thickness is accounted for.

	Entry [mm]	Exit [mm]
Horizontally (x)	-57, +57	-97, +97
Vertically (y)	-62, +25	-145, +35

In the z-direction the guide is 3.48 m. 3 mm needs to be left between the start of the monolith wall and the guide, and 17 mm at the end.

For the guide downstream there are practically no constraints, except for cost and feasibility.

For the results presented in the following sections it holds that:

- The m-value used for calculations is $m = 4$, with the exception of the Venetian blinds and the curved guide (see sections 5.1.2 and 5.2.2). As seen in figure 3.4, the performance can increase with higher m, but so will the manufacturing cost [43]. $m = 4$ is a valid choice for this type of focusing guide to get a good tradeoff between cost and performance [43].
- The default McStas values for low-angle reflectivity, critical scattering vector, slope of reflectivity and width of supermirror cut-off are used, with the exception of the curved guide (see section 5.2.2).
- When referring to "the target" in the following sections, an annihilation target is meant (see section 3.4). Its diameter is either 1 m or 0.4 m. The target is placed 65 m away from the moderator.
- All FOM plots and values are given at the target position. The plots are shown for the 5×3 m^2 so called target screen (cf. section 4.4).
- 1 ILL unit is $2 \cdot 10^9$ n·s (see section 2.1.3).
- Simulations were run for the wavelength interval 0.1 Å to 20 Å.
- The number of simulated tracks was 10^6, except for the generation of wavelength and velocity distribution plots were it was 10^8. The McStas setting for seed was set to 1.
- 2 MW power for the ESS linear accelerator was used.

5.1 Guide for antineutron searches

The guide system to study $n - \bar{n}$ oscillations will be built up of two separate optics pieces: one monolith guide and one downstream optics component. These are detaild in sections 5.1.1 and 5.1.2 respectively. The elliptic guides were constructed using equation (3.3).

5.1.1 Elliptic monolith guide

Due to the asymmetric constraints of the NBOA and the symmetry of the moderator (see section 3.3), the common choice of a focusing ellipse was generalized to a four-sided elliptic guide with a rectangular cross section. This will be called the elliptic monolith guide (EMG). This meant that four different values for the semi-axes a and b were used; top and bottom in the yz-plane and left and right in the xz-plane. The focal points were the same for all elliptic sides; one coinciding with the moderator focal point at the `McStas` origin (see figure 4.2) and one at the annihilation target. A drawing of the guide is shown in figure 5.1 and a view of the guide implemented in McStas is seen in figure 5.2.

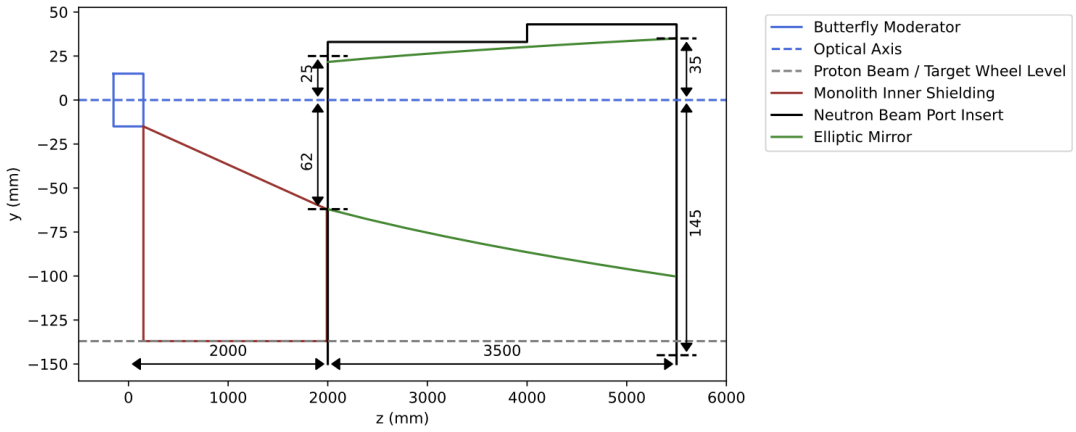

(a) Side view.

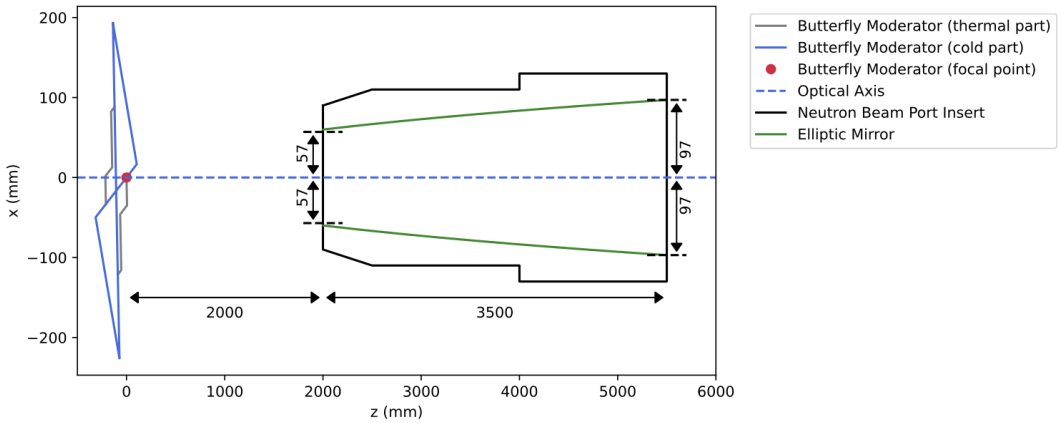

(b) Top view.

Figure 5.1: 2D drawings of the EMG together with the NBPI and the moderator.

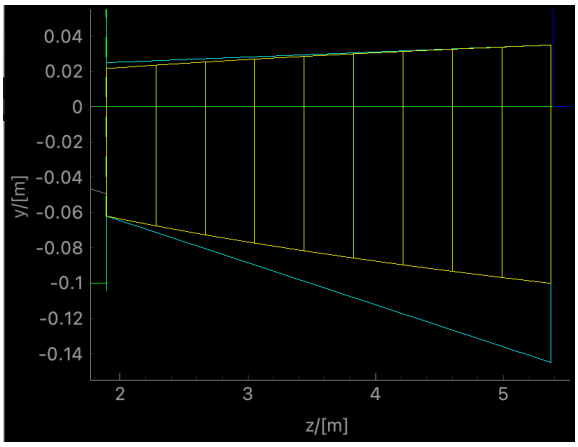

(a) Side view of the guide.

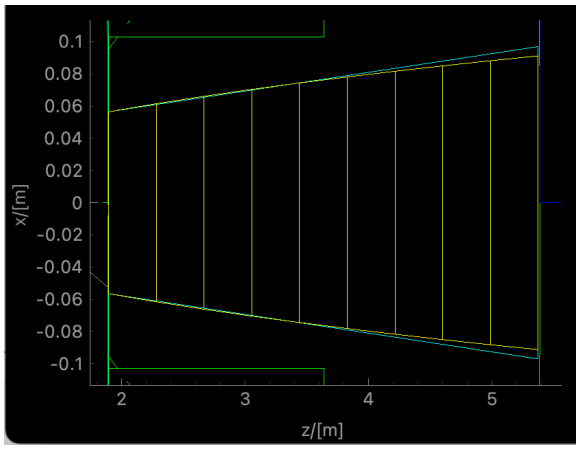

(b) Top view of the guide.

Figure 5.2: The EMG seen in McStas. The turquoise shape is the constraints, the elliptic guide is shown in yellow.

The construction of the ellipses was made with a code that optimized the largest possible asymmetric ellipse with the given constraints and the desired focal points. In 5.2 one can see that the guide is divided into 9 segments; this is a result of the scheme to construct the guide which consisted in the piece-wise addition of trapezoids. For all four ellipses except the top one the entrance constraints are the limiting ones, which can be seen in figure 5.2.

The focal length is $f = 32.5$ m for all elliptic sides of the guide, corresponding to half the moderator-target distance. The semi-major and semi-minor axes for the respective ellipses are given in table 5.2. The exact dimensions of the guide are given in table 5.3.

Table 5.2: Values of the semi-axes for the four-sided elliptic monolith guide. Since the constraints are symmetric in the horizontal direction, the values for the right and left ellipses are the same.

	a [m]	b [m]
Top	32.5000621	0.063547134
Bottom	32.5005225	0.184303995
Right/Left	32.5004417	0.169444074

Table 5.3: Dimensions of EMG (cf. table 5.1).

	Entry [mm]	Exit [mm]
Horizontally (x)	-57, +57	-93, +93
Vertically (y)	-62, +21	-102, +35

Running simulations with this guide in McStas yields the values shown in tables 5.4 and 5.5. In figure 5.3 is seen the FOM distribution at the target screen with a 1 m diameter target. In figures 5.4a and 5.4b the velocity- and wavelength distributions in the target are plotted.

Table 5.4: Results for EMG. The values from the ILL are inserted for comparison. The target diameter used is 1 m.

	Monolith guide at HIBEAM	ILL [19]
Total neutron current in target [n/s]	$(1.51 \pm 0.01) \cdot 10^{12}$	$(1.25 \pm 0.06) \cdot 10^{11}$
FOM [n·s]	$(1.52 \pm 0.01) \cdot 10^{9}$	$2 \cdot 10^{9}$
FOM ratio ILL	0.762	1
Optimum target center x [m]	0.429	-
Optimum target center y [m]	-0.0190	-
Average wavelength [Å]	3.1	5.9
Average velocity [m/s]	1500	670
Average time of flight [s]	0.050	0.109

Table 5.5: FOM values for the EMG with two different target sizes.

	1 m ⌀ target	0.4 m ⌀ target
FOM in target [n·s]	$(1.52 \pm 0.01) \cdot 10^9$	$(3.57 \pm 0.05) \cdot 10^8$
FOM ratio ILL	0.762	0.179

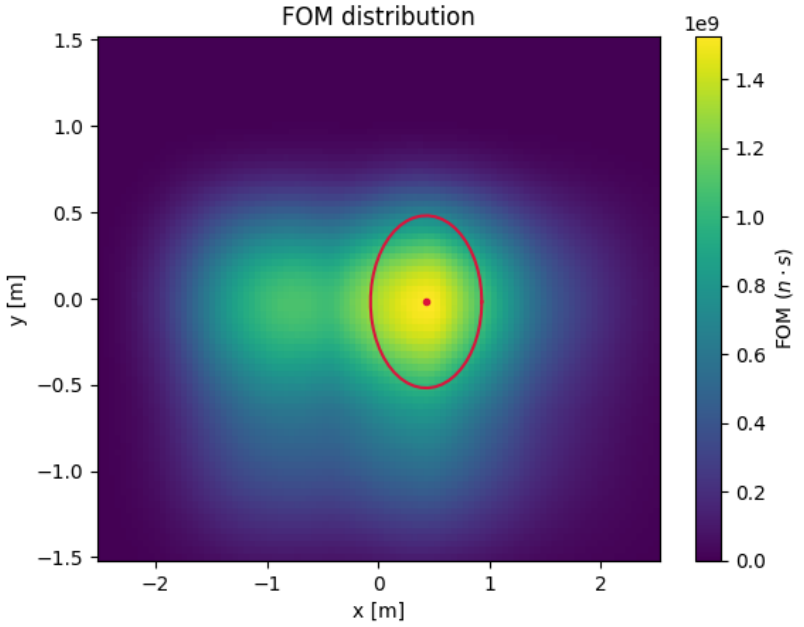

Figure 5.3: FOM distribution for the EMG. The red circle is placed at the position where the highest FOM value can be obtained for an annihilation target with 1 m diameter.

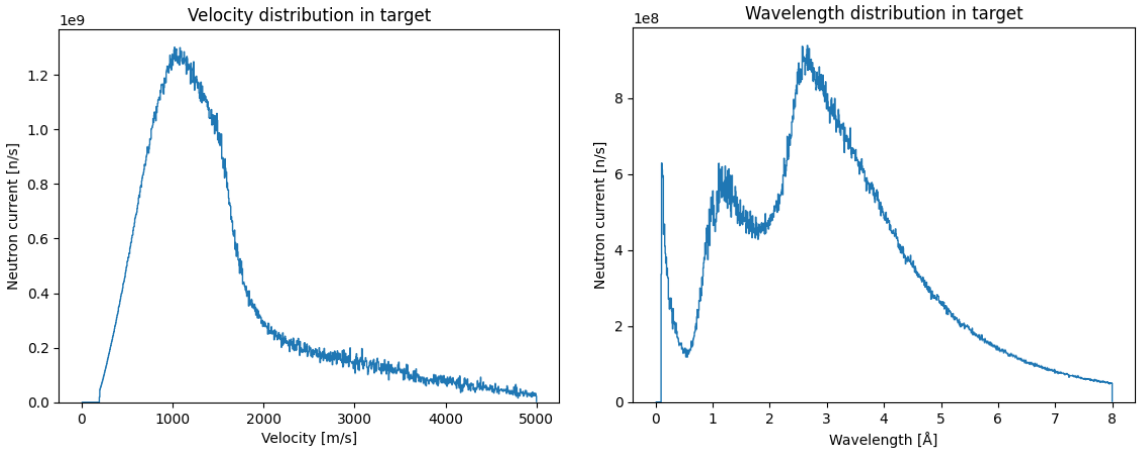

(a) Velocity distribution.

(b) Wavelength distribution.

Figure 5.4: Velocity and wavelength distributions for the EMG in a 1 m diameter target. To reduce the impact of statistical fluctuations, the number of tracks for this simulation was increased to 10^8.

As seen in figure 5.3, neutrons hitting the screen are not well focused inside the imaginary target (red circle). In fact there seem to be two maxima, which might relate to the symmetry of the moderator and the fact that most neutrons are not emitted exactly parallel to the beamline. It is however apparent that a larger target area makes a considerable difference; the FOM in a 0.4 diameter target is only ca 23% of the FOM in the 1 m diameter target, as seen in table 5.5. This scales roughly as the ratio of the target areas (the expected value being 16%).

The FOM distribution in figure 5.3 will in the following section be analysed in more detail with respect to the known properties of the moderator, specifically the extraction of cold and thermal neutrons (see figure 3.8). To do this, the `McStas` component `slit` was used. The function of the `slit` is illustrated with the following inequality statements;

```
if xmin <= x <= xmax and ymin <= y <= ymax: transmission
else: no transmission
```

i.e. there is a specified window in which tracks are allowed to propagate but outside this no transmission is allowed. In this case, the size of the window was 0.5 m in the x-direction, which was the relevant direction for looking at cold vs thermal neutrons. In the y-direction the slit window was sufficiently big to not interfere with the neutron extraction. The `slit` was placed 0.5 m from the moderator in z-direction but the positioning in the x-direction varied in the two cases as can be seen in figures 5.5 and 5.7.

Cold part

The extraction point for cold neutrons at the E6 beamline is at the "top" part of the moderator when seen in the top view, see figure 4.2. To look primarily at the cold part of the neutron spectrum, the contribution from thermal neutrons was reduced by blocking the lower part of the moderator, which yields thermal neutrons, with the `slit`. See figure 5.5

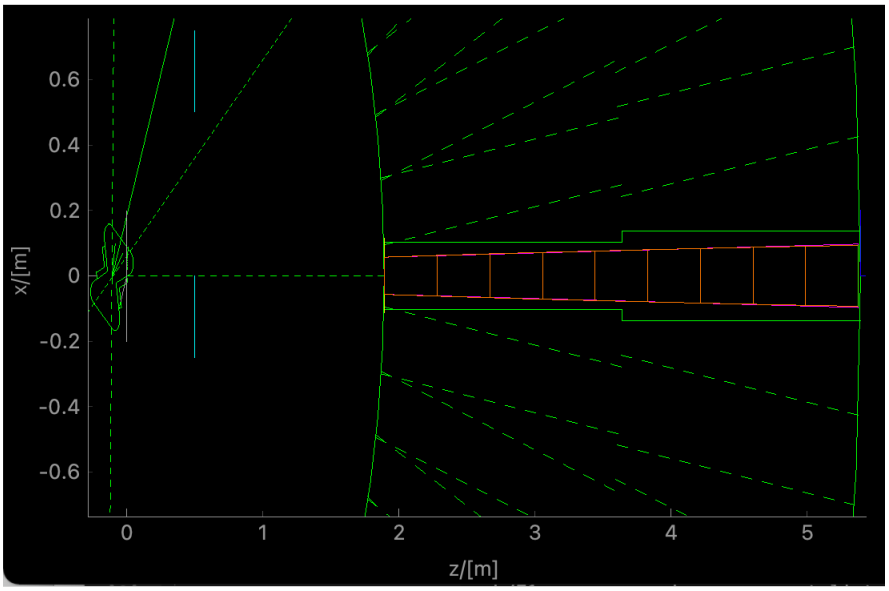

Figure 5.5: Overview of the setup with a `slit` close to the moderator to reduce the contribution from thermal neutrons. The `slit` window is wide and not blocking anything in the yz-plane.

The optimal FOM value in a 1 m diameter target is here $1.26 \cdot 10^9$ n·s. This is 83% of the value for the whole spectrum. This means that the largest contribution to the FOM value comes from the cold neutrons. The FOM distribution is shown in figure 5.6.

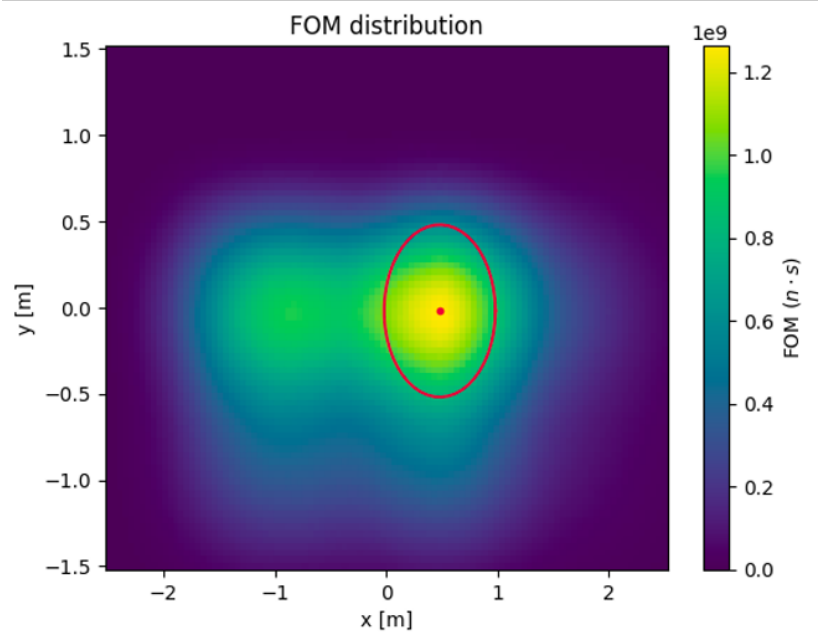

Figure 5.6: FOM distribution for the cold part of the neutron spectrum. The target diameter used is 1 m.

Thermal part

The slit is now moved to instead block the upper part of the moderator to filter out the cold neutrons, see figure 5.7.

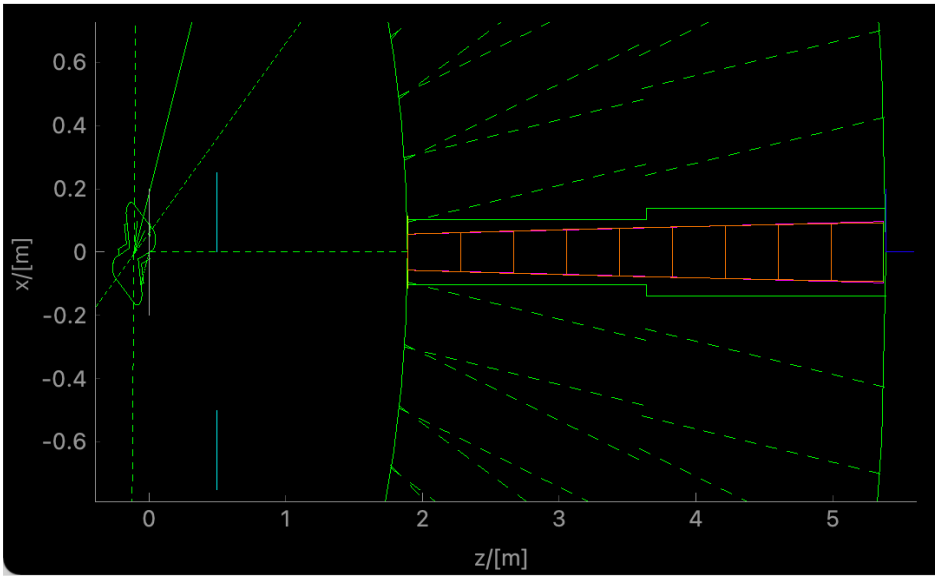

Figure 5.7: Setup with the `slit` to reduce the cold neutron contribution. The `slit` window is wide and not blocking anything in the yz-plane.

The best FOM value is $2.79 \cdot 10^8$ n·s in this case, which is only a small part of the total value. The FOM distribution is shown in figure 5.8.

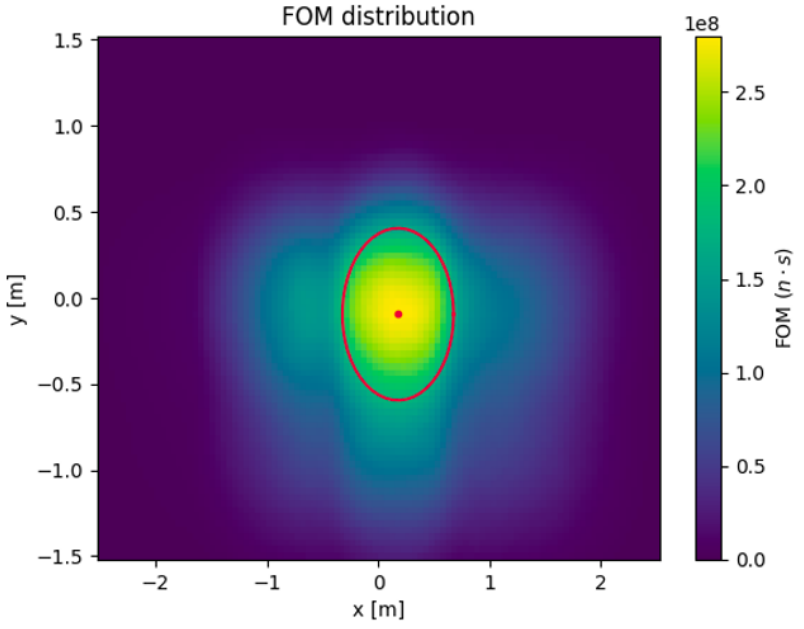

Figure 5.8: FOM distribution for thermal neutrons. The target diameter used is 1 m.

The result that cold neutrons contribute more to the FOM than thermal neutrons is expected. This analysis also shows that the upper part of the moderator as seen in the top view is the most valuable for neutron oscillation experiments at beamline E6.

5.1.2 Downstream optics

For the downstream optics, some different possibilities were explored. Since the surroundings were less restrictive here than for the monolith guide, more freedom in regards to dimensions and geometry was available. The first option investigated was an extension of the elliptic monolith guide. Secondly, tests were run with a nested mirror system referred to as Venetian blinds.

To study the guide system which would yield the best FOM in target, the second guide was placed at a distance of 70 cm from the monolith wall on the optical axis. This was needed to leave space for the shutters.

Second elliptic guide

This second elliptic guide was as said an extension of the EMG and the construction procedure was the same for this one as for the EMG. To find the best shape of the guide, optimization of two parameters was made: the length of the guide and the so called margin of the guide. Since there is a free space of 70 cm between the end of the EMG and the start of the second guide, neutrons will be lost in this area. To mitigate the neutron loss, one possibility is to increase the entry dimensions of the second guide. Therefore a margin parameter was added which made the guide a few millimeters wider on each side. A margin of 0 m means that the entry dimension for the second guide are the values the EMG would have had if it had continued to the starting position of the second guide. See figure 5.9 for an illustration of how the margin parameter was implemented.

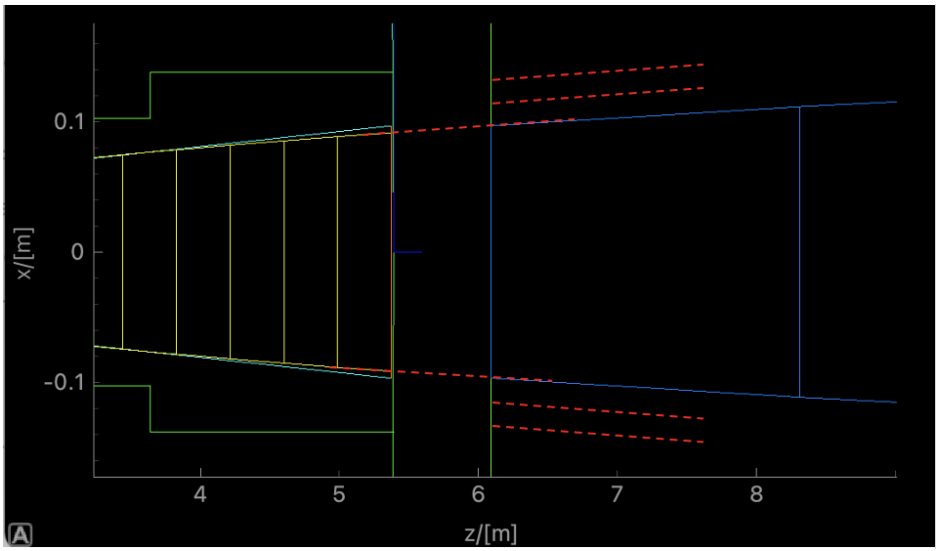

Figure 5.9: Illustration of the addition of the margin parameter to the second guide (dark blue). Red dashed lines represent different values of the margin. The same margin was added on all sides in both the top view (shown) and the side view.

The optimization scheme was first run for the annihilation target with a diameter of 1 m. First, the length of the second guide was optimized, with the margin set to 0 m. After this, the margin was varied while the length was set to the obtained optimum value. The results of the optimization are seen in figure 5.10.

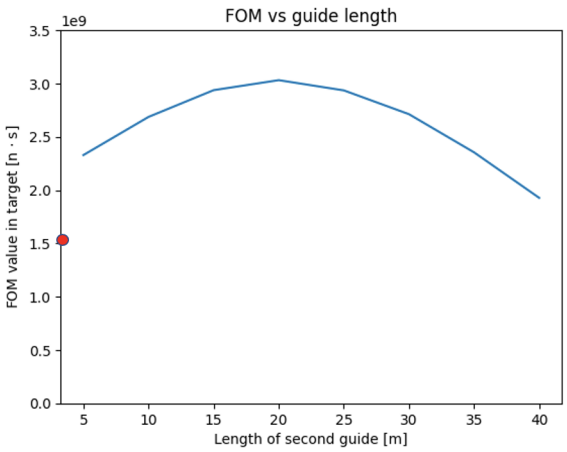

(a) Length optimization. The red dot points out the FOM value without the second guide. Margin is set to 0 m.

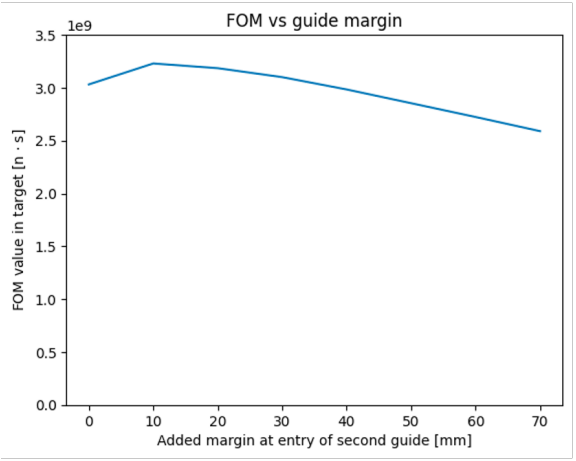

(b) Margin optimization. The length was 20 m.

Figure 5.10: Optimization of FOM in a 1 m diameter target for the second elliptic guide.

From figure 5.10 one can discern that the optimal FOM value is obtained when the second guide is about 20 m long, with an added margin of 10 mm on each of the four sides of the guide. This is then the optimal trade-off between good focusing and long

uninterrupted flight time. The semi-axes of this elliptic guide can be found in table 5.6 and its entry and exit dimensions in table 5.7. The focal length was as before $f = 32.5$ m.

Table 5.6: Values of the semi-axes for the 20 m long four-sided elliptic second guide with a 10 mm margin. Again, the constraints are symmetric in the horizontal direction so the values for the right and left ellipse sides are the same.

	a [m]	b [m]
Top	32.5001000	0.080625020
Bottom	32.5006230	0.201229159
Right/Left	32.5005345	0.186388101

Table 5.7: Dimensions of the second elliptic guide with optimal parameters.

	Entry [mm]	Exit [mm]
Horizontally (x)	-107, +107	-188, +188
Vertically (y)	-116, +47	-203, +82

A picture of the second guide with the optimal parameters is shown in figure 5.11. The results for the setup with the EMG and the optimized second guide can be found in table 5.8. The FOM distribution is shown in figure 5.12.

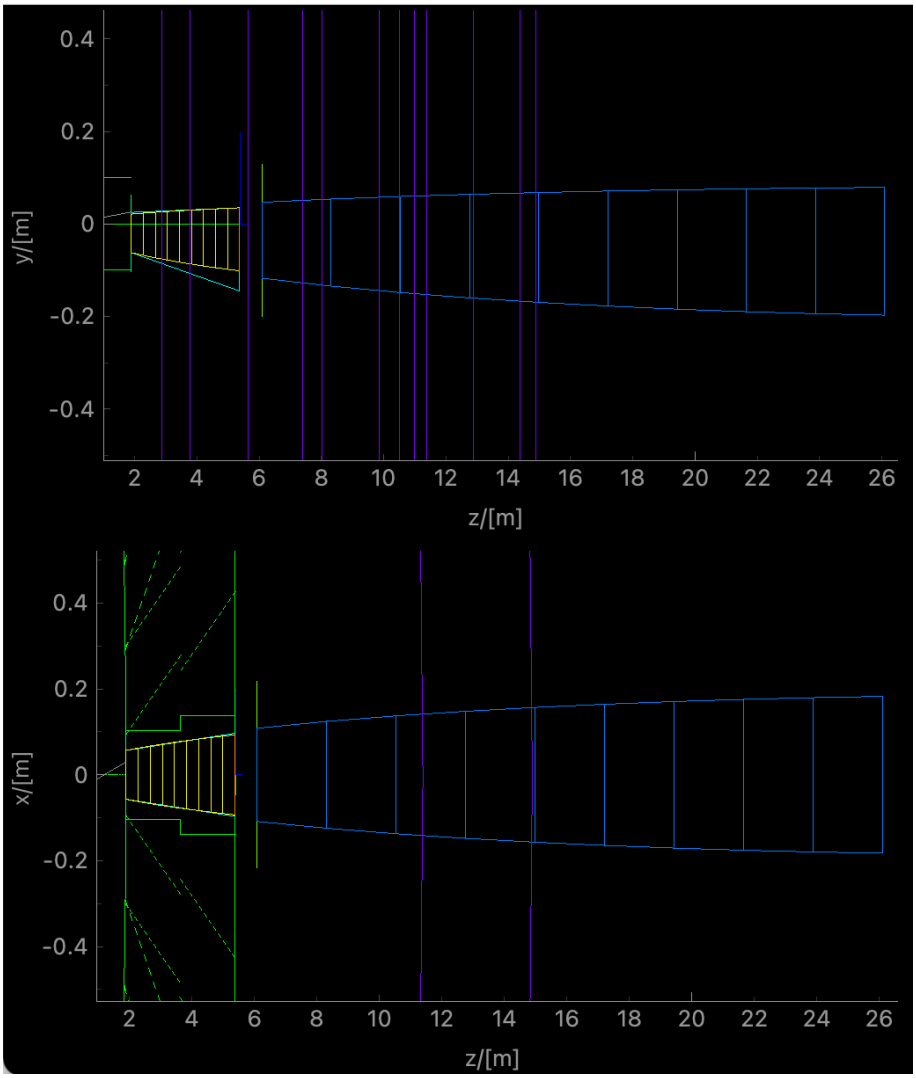

Figure 5.11: The EMG together with the optimized second elliptic guide. The latter has a length of 20 m and margin of 10 mm on each side.

Table 5.8: Results for the setup with the EMG and the optimized second elliptic guide. The results are compared with the ones obtained only with the EMG. The target diameter used is 1 m.

	With second elliptic guide	Only monolith guide
Total neutron current in target [n/s]	$(1.134 \pm 0.008) \cdot 10^{12}$	$(1.51 \pm 0.01) \cdot 10^{12}$
FOM [n·s]	$(3.23 \pm 0.01) \cdot 10^{9}$	$(1.52 \pm 0.01) \cdot 10^{9}$
FOM ratio ILL	1.61	0.762
Optimum target center x [m]	0.0253	0.429
Optimum target center y [m]	-0.0570	-0.0190
Average TOF [s]	0.049	0.050

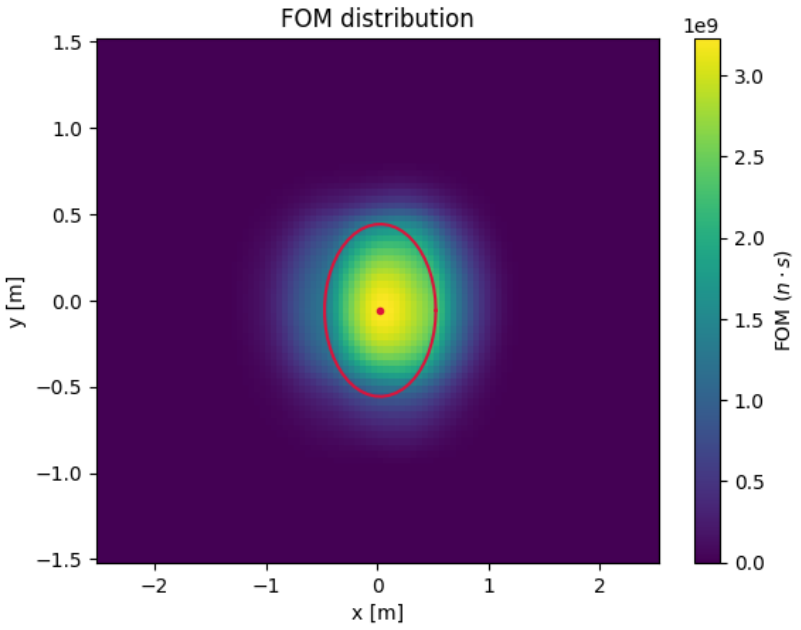

Figure 5.12: FOM distribution for the setup shown in fig 5.11. The target diameter is 1 m.

A similar optimization scheme was then performed for a size of the annihilation target of 0.4 m in diameter. The margin was kept to 10 mm on all sides while the length was varied. The result was that a slightly longer guide, 35 m, would give the best FOM value. This was expected since a longer guide implies better focusing, which was needed in the case of the smaller target. The result together with a comparison between the different target sizes can be found in table 5.9.

Table 5.9: FOM values for the setup with the EMG and the optimized second elliptic guide for two different target sizes. For the 1 m target, the length of the second guide was 20 m and for the 0.4 m target it was 35 m. The margin for the second guide was 10 mm in both cases.

	1 m ⌀ target	0.4 m ⌀ target
FOM [n·s]	$(3.23 \pm 0.01) \cdot 10^9$	$(1.46 \pm 0.01) \cdot 10^9$
FOM ratio ILL	1.61	0.658

Comparing figure 5.12 with figure 5.3, a major improvement in the focusing has been achieved as now most of the neutrons hit the target screen in the intended target area. The total neutron current recorded on the 5×3 m^2 screen is less for the setup with two guides than with only the EMG. This is expected since most neutrons will interact with the mirror material of the second guide at least once and a part of them will then be lost in the material. The FOM however has more than doubled after the addition of the second guide.

An interesting result is that the time of flight has not been drastically reduced by the introduction of the second elliptic guide, as shown in table 5.8. This had been expected, since neutrons that are reflected in the second guide will have their TOF reset and have a shorter free flight path. However, the loss in flight path is somewhat compensated by the fact that neutrons that are reflected in the second guide on average have a lower velocity (see section 3.2.1). A similar study of wavelength and velocity distributions as was shown for the EMG in figure 5.4 was made for the setup with the EMG and the optimized second guide (see appendix A.1). A mean velocity of 1400 m/s was obtained, to be compared with 1500 m/s for only the EMG. The neutrons that hit the target in this case will therefore still have a time of flight comparable to the one obtained without downstream optics.

Again, a comparison between the FOM values for different target sizes can be made. This is seen in table 5.9. In this case the smaller target yields a FOM of 45% of that of the larger one. This is an improvement from the previous case were the ratio was 23%, which testifies once more to the good focusing properties of the second elliptic guide.

Instead of adding a margin to the second guide to increase the collection of neutrons, one could have introduced a "shutter guide" which would cover the space between monolith wall and start of the second guide when the shutters are not in place. This was tried out but the gain was at most around 5%, which was less than the gain of using a 10 mm margin.

Venetian blinds

For more in depth details about the `McStas` component `Venbla`, see [41]. See also [28] for more details about nested mirror systems.

The Venetian blinds (VB) was constructed to have a focusing window of ± 2 m at 75 m from the moderator.[1] The so called height of the VB array (hvb) would then have to be adjusted with the z-position of the component (zvb), which is shown in figure 5.13. For simplicity also the width (wvb) was adjusted so hvb = wvb. The detector height parameter determines the size of the "free region" where no blades will be placed. Since the FOM distribution for the EMG was more spread out in the horizontal direction (see figure 5.3), a Venetian blinds component was placed to focus the beam in the x-direction, so that the blades were parallel to the y-axis.

The construction of the blades for the VB component is an iterative process. First the blade array for positive x-values are defined, and these are later mirrored for the

[1] The original plan was to have the HIBEAM experiment at the E5 beamline, which would be 75 m long. Due to complications with a loading platform for trucks at the would be detector site of E5, the proposition to move to E6 was made.

negative x-values. The position and angle of the first blade is calculated given hvb, zvb, and z-position of the detector to get reflection to $(x, z) = (0, 65)$. The next blade is placed so that its top left corner intersects the ray going from the source to the bottom right corner of the previous blade. This is illustrated in figure 5.14. The number of blades used by the `Venbla` component is therefore dependent on hvb, zvb and height of the detector as well as the length and thickness of the blades.[44]

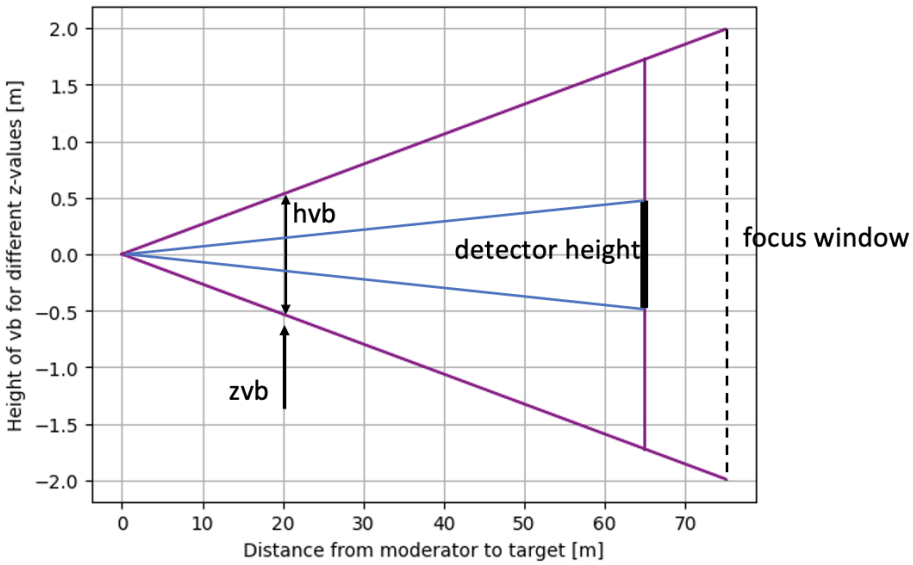

Figure 5.13: The concept of the VB component used in the project. The relation between zvb (on x-axis) and hvb (on y-axis) is shown. The vertical line at $x = 65$ m indicates the target location for the E6 beamline, with the detector height marked out. The blue lines determined by this parameter limit a space in which neutrons can pass from the moderator to the target unperturbed; no blades will be put in this region since reflection is not required here. At $z = 75$ m the focusing window is shown.

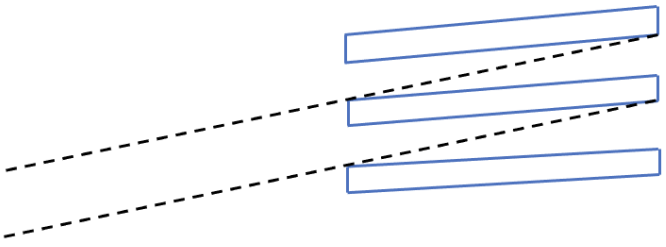

Figure 5.14: Illustration of the construction of the blades of the Venetian blinds. The black lines are thought to continue towards a source in the bottom left corner. The first blade is placed with its center at a height of hvb/2 from the optical axis, the second is then placed underneath so that its top left corner intersects a ray from source to the bottom right corner of the previous blade.

As was the case with the second elliptic guide, an optimization of the FOM value in a 1 m diameter annihilation target was made for a few parameters to find the best setup. The optimized parameters were z-position zvb and blade length (len). First zvb was optimized; the blade length used was then 30 cm which was the recommended default value [44]. An optimization loop was then run for the blade length with the obtained optimum parameter for zvb.

In table 5.10 are listed the required parameters that were kept constant during the optimization procedure.

Table 5.10: The required parameters that were kept constant during the optimization.

Parameter	Value
z-position detector [m]	65
blade thickness [m]	0.002
detector height [m]	1
m-value	6
x-position detector [m]	0

In figure 5.15 the results of the optimization procedures are shown. The optimum position for the VB optics is at about $z = 22$. This placement means that reflected neutrons have a shorter flight path than if the VB had been placed closer to the monolith. A location close to the monolith however would have meant that the entire component would be smaller, meaning that the blade thickness would have had a larger effect and a greater portion of the neutrons would have been absorbed by the blades. Regarding the blade length, there is a slight gain when extending the guide but this comes with mechanical complications; the blades can for example start bending downwards because of gravitational effects (see section 3.2.3). The gain in FOM when using 50 cm blades instead of 30 cm is less than 3%. The optimal configuration was chosen as zvb = 22 m and len = 0.3 m; this setup is shown in McStas in figure 5.16. The number of blades created for this configuration was 150.

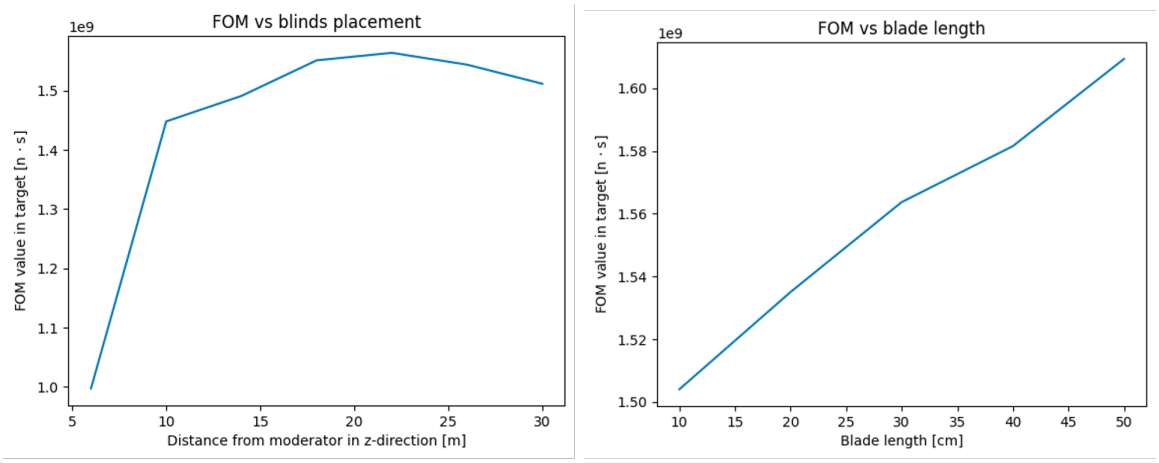

(a) FOM value in target as a function of the z-position of the VB. The blade length was set to 30 cm.

(b) FOM value in target as a function of the length of the blades. The z-position was 22 m.

Figure 5.15: Parameter optimization for the Venetian blinds. Note that the y-axes are different in (a) and (b).

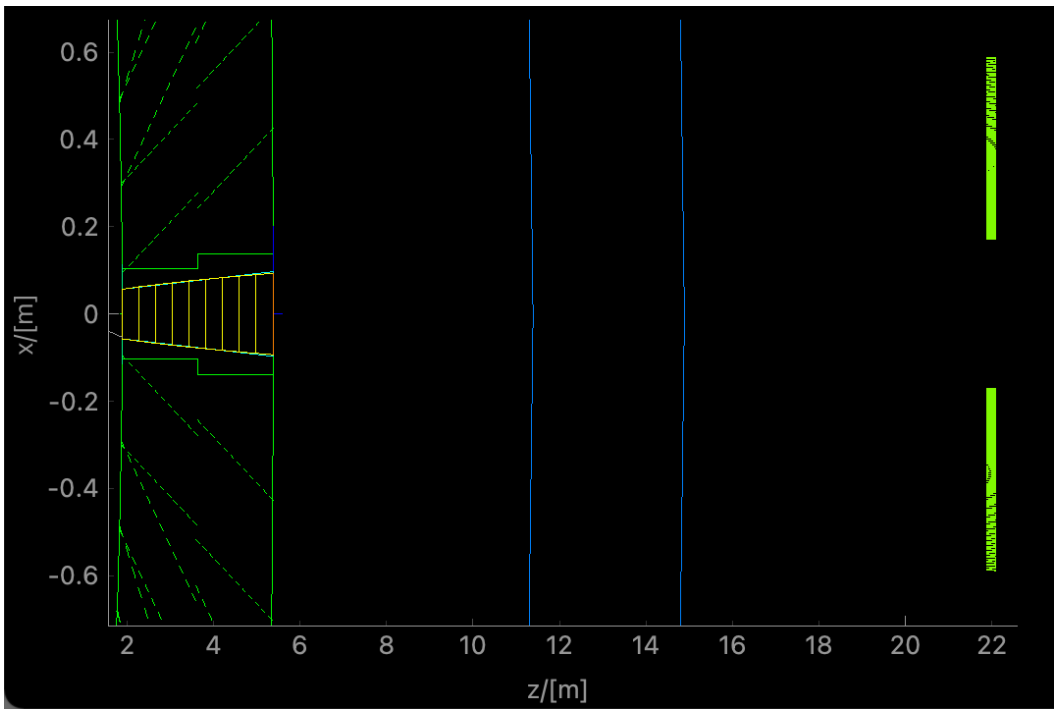

Figure 5.16: Top view of the Venetian blinds with the optimal parameters for blade length and z-positioning together with the elliptic monolith guide.

The results, compared with the values for the second elliptic guide, are displayed in table 5.11. The FOM distribution for the optimised VB component is shown in figure 5.17.

Table 5.11: Results for the setup with the elliptic monolith guide and Venetian blinds with optimal parameters. The results are compared with the ones for the other possible downstream optics component together with the EMG.

	EMG + Venetian blinds	EMG + second elliptic guide
Total neutron current in target [n/s]	$(1.025 \pm 0.009) \cdot 10^{12}$	$(1.134 \pm 0.008) \cdot 10^{12}$
FOM [n·s]	$(1.57 \pm 0.01) \cdot 10^{9}$	$(3.23 \pm 0.01) \cdot 10^{9}$
FOM ratio ILL	0.783	1.61
Optimum target center x [m]	0.126	0.0253
Optimum target center y [m]	-0.0570	-0.0570
Average TOF [s]	0.048	0.049

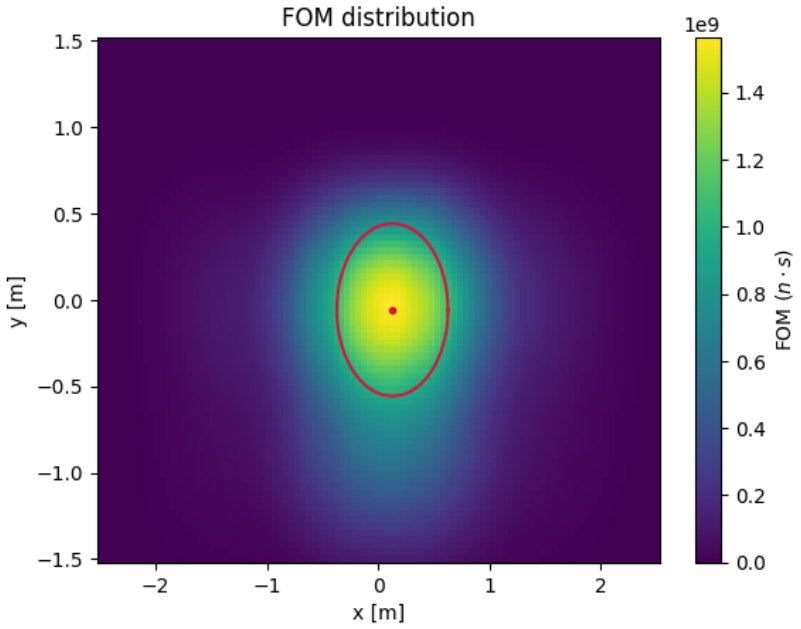

Figure 5.17: FOM distribution for a 1 m diameter target with VB placed at $z = 22$ m and blade length 30 cm.

From table 5.11 it is clear that the second elliptic guide performs better. The Venetian blinds barely improve the FOM value obtained with only the EMG, which was $1.52 \cdot 10^9$. There are however several problems with the VB component in its current execution. Firstly, the blade thickness used was 2 mm which is relatively thick. In [29], the thickness used was 0.15 mm, but their blades were also considerably smaller than the proposed dimensions in this study. Secondly, a large number of blades were used which were put closely together. Together with the considerable blade thickness, this meant that there was not much space left for neutrons to pass through the blinds array, unless they had already been focused by the EMG and traversed the VB component in the free region. Furthermore, this analysis was made only for Venetian blinds in the horizontal direction which means it is not entirely fair to compare it with the second elliptic guide. This would be more like an elliptic guide with only the left and right sides and no top and bottom. From figure 5.17 one can see that there is some focusing

lacking in the vertical direction, even though most of the FOM in fact already is in the target. Adding another VB component with 2 mm thick blades could probably also hurt more than help, since more neutrons would be lost.

5.1.3 Conclusion: $n - \bar{n}$ guide

It has here been shown that with an elliptic monolith guide together with a 20 m long second elliptic guide, both with $m = 4$, and an annihilation target size of 1 m in diameter, the previously best FOM value for free $n - \bar{n}$ searches obtained at ILL can be improved at the 65 m long HIBEAM beamline at ESS, using an accelerator power of 2 MW. The ILL:s maximum flight path was longer and they used colder neutrons which helped them achieve a high sensitivity, but thanks to the high neutron current at ESS and good focusing optics, a similar and even slightly improved sensitivity could be reached with a shorter flight path and more energetic neutrons. As described in section 2.1.1, the FOM is proportional to the time of flight squared, so the fact that a better FOM than the ILL one can be obtained at this standard ESS beamline is not a trivial feat. With a longer beamline, colder neutrons and an even higher neutron current, which will be the case for NNBAR, the possible FOM that can be obtained will indeed be a great improvement of the ILL value; hopefully an increase of as much as three orders of magnitude.

In table 5.12 a comparison between some experimental parameters for the search for antineutrons at ESS (HIBEAM) and ILL can be found.

Table 5.12: Parameters of the 1994 ILL experiment [19] together with values at HIBEAM with the optimum optics configuration for $n - \bar{n}$ searches. Neutron current, uninterrupted time of flight and wavelength are measured at the target.

	Max. flight path [m]	Target diameter [m]	Neutron current [n/s]	Avg. free TOF [s]	Avg. wavelength [Å]	FOM [n·s]
HIBEAM	65	1.0	$1.13 \cdot 10^{12}$	0.0492	3.1	$3.2 \cdot 10^{9}$
ILL	81	1.1	$1.25 \cdot 10^{11}$	0.109	5.9	$2.0 \cdot 10^{9}$

Calculations were made for both a 1 m diameter target and a 0.4 m diameter target (see table 5.9). The difference in FOM in these cases is considerable; with a 0.4 m target, the value at the HIBEAM beamline is less than the ILL value, while with a 1 m target the FOM is more than one and a half times the ILL FOM. The larger detector is then preferable – its primary drawback would be the economic cost.

5.2 Guide for sterile neutron searches

The guide system for the $n - n'$ experiment will, as in the $n - \bar{n}$ case, consist of one guide in the monolith and one downstream optics component. The latter will be a curved guide, as mentioned in section 2.1.4. Since the advantage of using focusing optics in the monolith is not obvious in this case, a more simple option was tried; a monolith guide with straight sides. This concept will be called the tapered monolith guide and it will be explained properly in section 5.2.1.

In section 5.2.2, the design and development of the curved guide will be presented. The complete guide system for $n - n'$ searches will then be outlined in section 5.2.3.

5.2.1 Tapered monolith guide

The tapered monolith guide is another option for the NBOA that might be better suited for the search for sterile neutrons. To meet the constraints but still collect as many neutrons as possible, it was made larger at the exit than at the entrance; hence the name tapered. For simplicity, the divergence will be the same for both sides of the guide in one plane. That is, in the xz-plane, the guide will be symmetric around the optical axis and in the yz-plane it will be shifted downwards with respect to the optical axis but be symmetric around its own center. See figure 5.18.

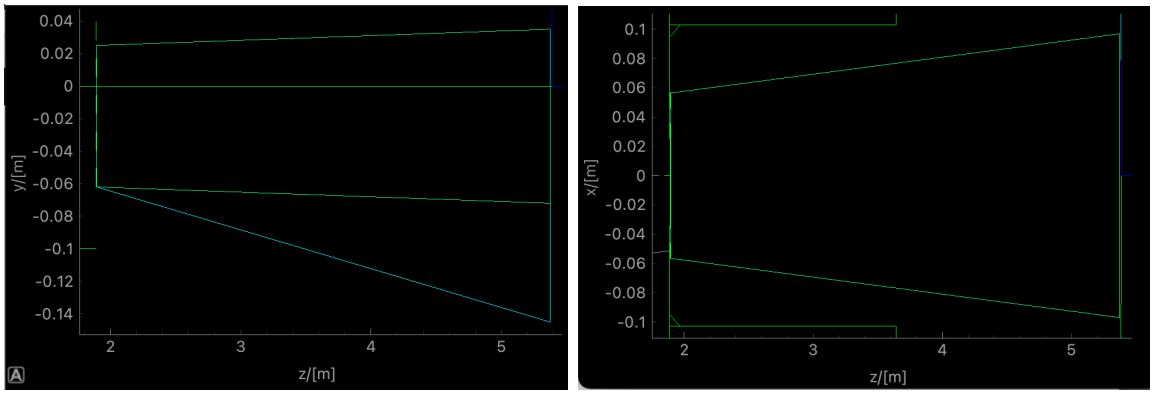

(a) Side view of the guide.

(b) Top view of the guide.

Figure 5.18: The monolith insert seen in McStas. The turquoise shape is the constraints, the rectangular guide is shown in green.

The dimensions of the tapered guide are displayed in table 5.13. Comparing with the engineering constraints in table 5.1, this guide fills all the available space in three of four directions. Only in the negative y-direction it is (considerably) smaller than the allowed value.

Table 5.13: Dimensions for tapered monolith guide (cf. tables 5.1 and 5.3).

	Entry [mm]	Exit [mm]
Horizontally (x)	-57, +57	-97, +97
Vertically (y)	-62, +25	-72, +35

In analogy to section 5.1.1 where the performance of the elliptic monolith guide for $n - \bar{n}$ searches was evaluated, the results of the tapered guide can be seen in table 5.14, together with a comparison with the EMG. The FOM distribution is shown in figure 5.19.

Table 5.14: Results of the tapered monolith guide, compared with the ones for the EMG.

	Tapered monolith guide	EMG
Total neutron current in target [n/s]	$(1.28 \pm 0.01) \cdot 10^{12}$	$(1.51 \pm 0.01) \cdot 10^{12}$
FOM [n·s]	$(1.09 \pm 0.01) \cdot 10^{9}$	$(1.52 \pm 0.01) \cdot 10^{9}$
FOM ratio ILL	0.543	0.762
Optimum target center x [m]	0.328	0.429
Optimum target center y [m]	-0.285	-0.0190
Average TOF [s]	0.055	0.050

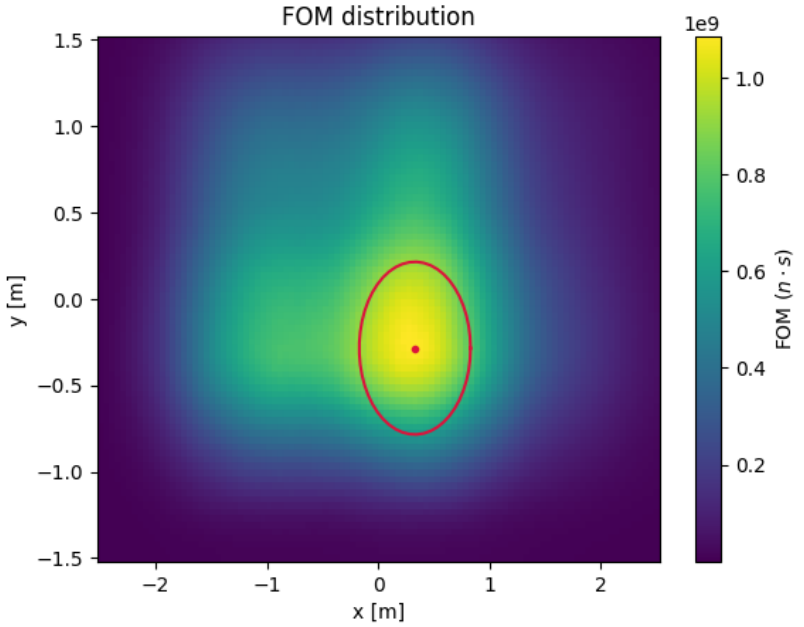

Figure 5.19: FOM distribution for the tapered monolith guide in a 1 m diameter target.

As seen in picture 5.19, the beam has not been especially focused. The FOM value for the tapered guide is also lower than for the EMG which can be seen in table 5.14.

The FOM ratio between the two monolith guides is around 0.7. The fact that the FOM value is still relatively high for the tapered guide is primarily because most of the neutrons that hit the central maximum have not been scattered; this can be understood from the long TOF and the fact that the ideal positions of the target are similar for the EMG and the tapered guide.

5.2.2 Curved guide

The curved guide was inspired by the ANNI instrument [45]. This was an instrument proposed in 2015 which was not approved, but it remains as a valid design for a particle physics beamline at ESS. Since this design was already optimized, the concept and parameters that were used for ANNI functioned as a base for the development of the guide used in this project. The guide dimensions were however increased to get an increase in neutron current and the requirement to lose line of sight twice was loosened.

For the construction of the curved guide in `McStas`, the properties of the guide were set to the same values as the ANNI instrument had, which can be found in [45]. These involved low-angle reflectivity, critical scattering vector, slope of reflectivity and width of supermirror cut-off, as well as four different m-values for the four different sides of the guide and the use of so called channels. The channels helped greatly with the neutron transport through the guide since the incident angles became smaller. The bending takes place in the positive vertical direction; there is not much space to the sides of the beamline, see figure 2.2, so bending horizontally would interfere with the other instruments. The parameters for the curved guide that differed from the ANNI values were the dimensions of the guide. The height in the vertical (bending) direction was set to 0.10 m and the width in the horizontal direction was 0.15 m.

Since the dimensions of the guide were changed compared to the ANNI design, it was necessary to investigate how much bending was needed in order to lose LOS of the moderator at least once. A routine to check whether a guide consisting of two bender parts, curving in opposite directions and with different bending radii and lengths would lose LOS from a source was then developed [37]. The bender parts need to curve the same angle, in opposite directions, in order for the sides of the curved guide to be parallel to the xz-plane at the start and end of the guide. Since the angle of a circle segment θ is related to the circle radius R and the segment length s by

$$s = \theta R, \tag{5.1}$$

a constant ratio between the length and the radius can be fixed. This means that only three parameters need to be input: the radius and length of the first bender and the length of the second bender. The radius of the second bender part is then calculated with equation 5.1.

In figure 5.20 is depicted a curved guide which have, for all points at the exit of the guide, lost LOS of the moderator at least once. It is a rough sketch of the setup, with

the curved guide starting at $x = 0$ and the moderator being located at $x = -6.2$, but it provides the information needed in this case.

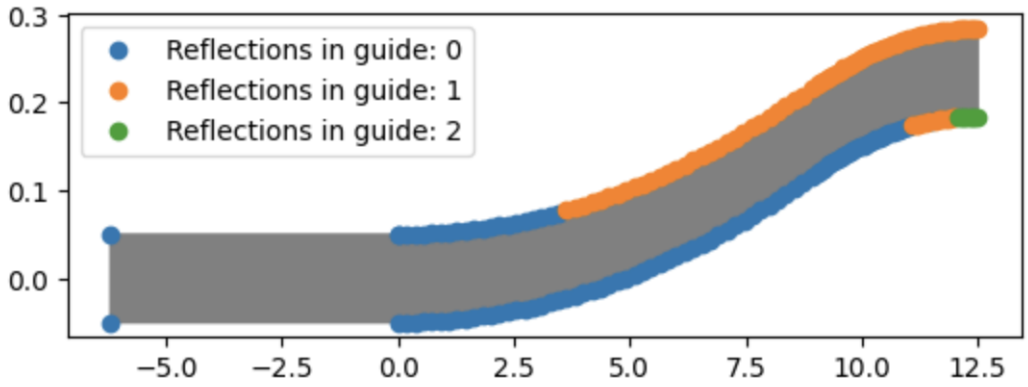

Figure 5.20: Sketch of the curved guide showing how many reflections are needed to get to the points on the sides of the guide. Blue dots show points in the guide that are within LOS of the moderator, i.e. no reflection in the guide is needed to get to this point. Orange dots can only be reached after having been reflected once in the guide and green points cannot be reached unless they have been reflected twice.

The parameters used which fulfill the requirement that LOS of the moderator needed to be lost at least once by the curved guide were

- Radius of first bender part $R_1 = 240$ m
- Length of first bender part $L_1 = 9$ m
- Length of second bender part $L_2 = 3.5$ m

The curved guide with these parameters is seen in the `McStas` coordinate system in figure 5.21.

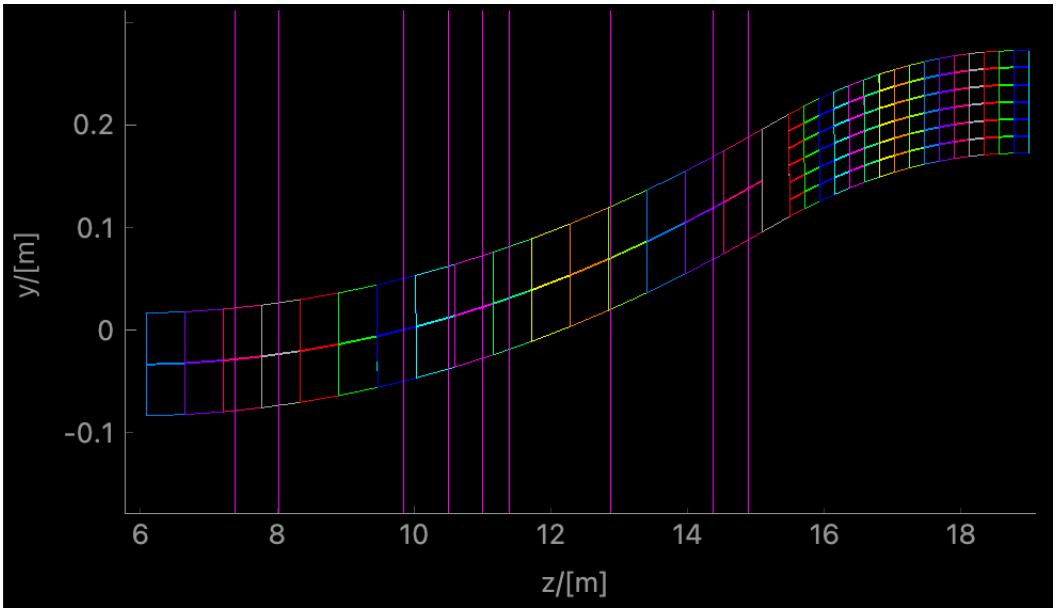

Figure 5.21: The curved guide as seen in the side view in `McStas`. The channels marked out divides the curved guide into smaller quadrangles.

5.2.3 Complete guide

The complete guide for a sterile neutron search at HIBEAM would consist of the tapered monolith guide and the curved guide. This is shown in figure 5.22.

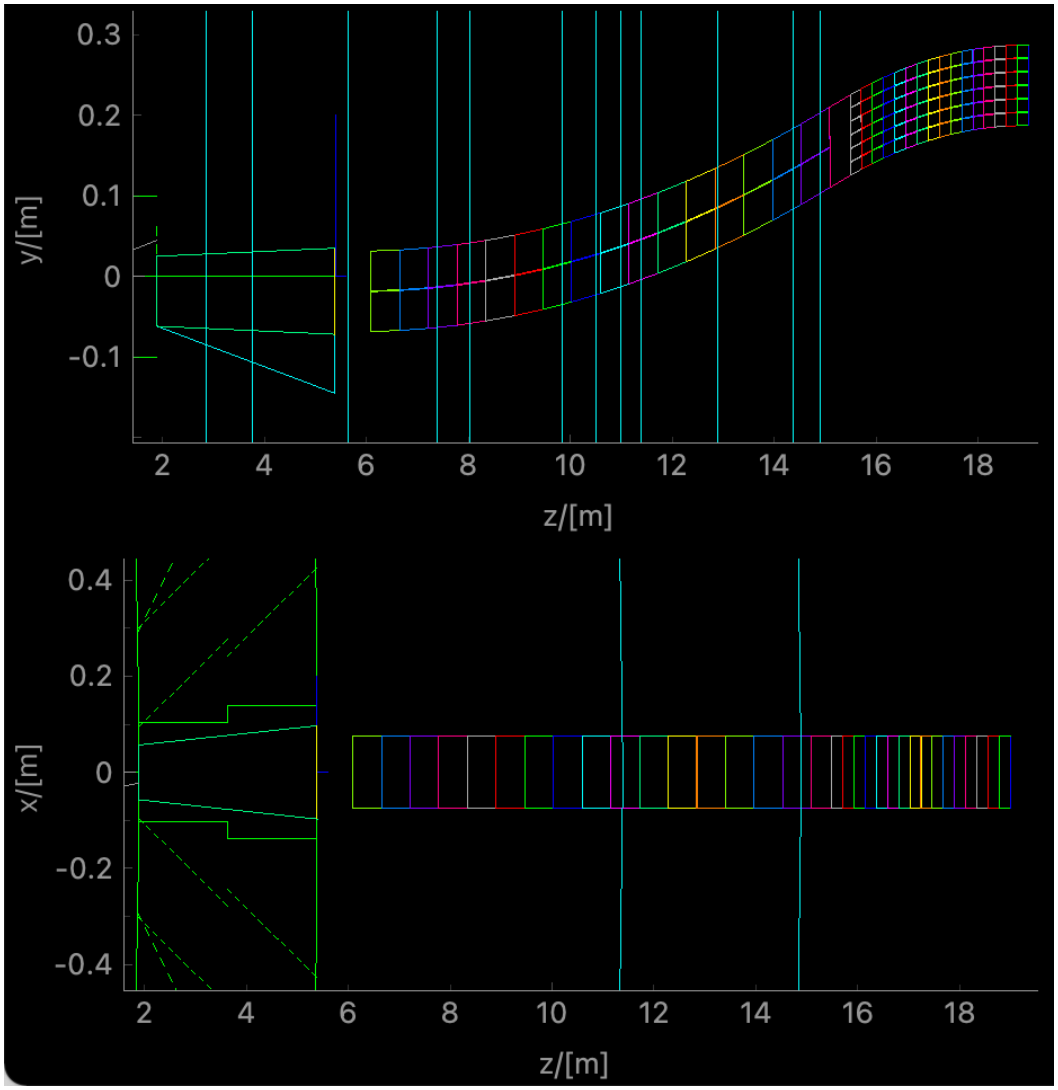

Figure 5.22: Setup with tapered monolith guide and curved guide.

From figure 5.22, one can see that the exit dimensions of the tapered guide and the entry dimensions of the curved guide are well matched in the side view and approximately matched in the top view.

The curved guide was also tried together with the EMG. This is seen in figure 5.23.

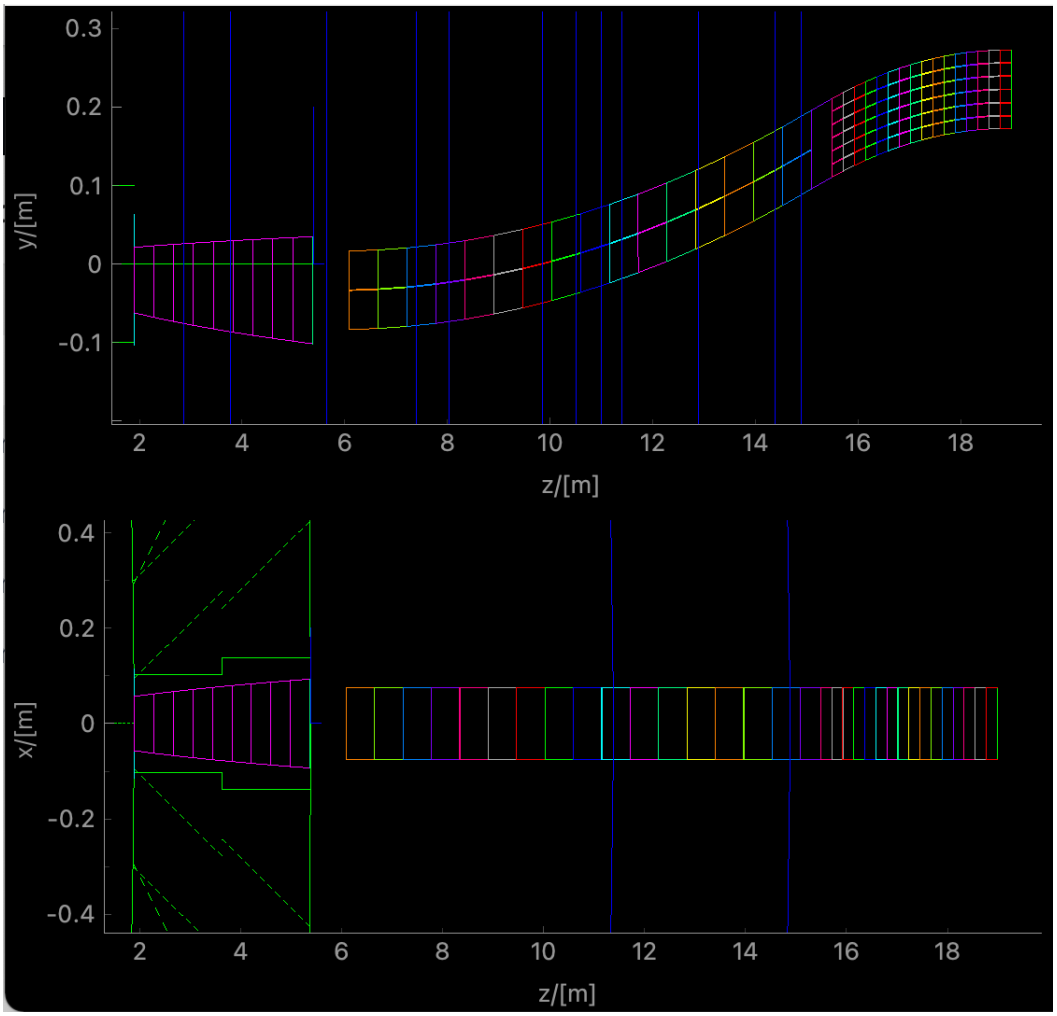

Figure 5.23: Setup with EMG and curved guide.

The results for these two different setups are found in table 5.15. The neutron currents were recorded with two 0.15 × 0.10 m^2 `PSD_monitors` placed at the entry and exit of the curved guide, plus a `PSD_monitor` at the exit of the monolith guide with dimensions matching the exit dimensions of the EMG or the tapered monolith guide.

Table 5.15: Results for the setup with a curved guide and the different NBOAs. The values given are neutron currents.

Neutron current → Type of monolith guide ↓	Exit monolith guide [n/s]	Entry curved guide [n/s]	Exit curved guide [n/s]	Ratio exit/entry curved guide
EMG	$(1.51 \pm 0.01) \cdot 10^{12}$	$(6.51 \pm 0.07) \cdot 10^{11}$	$(2.22 \pm 0.02) \cdot 10^{11}$	0.341
Tapered guide	$(1.30 \pm 0.01) \cdot 10^{12}$	$(7.63 \pm 0.07) \cdot 10^{11}$	$(2.48 \pm 0.02) \cdot 10^{11}$	0.325

As can be deduced from table 5.15, the tapered guide performs better. Both the neutron current at the entry of the curved guide and at the exit is higher for the

tapered guide. However, fewer neutrons are lost in the curved guide when using the EMG. This relates to the fact that the incident angles will on average be smaller in the EMG, since the focusing property of the ellipse leads to an overall reduction of the divergence with respect to the optical axis, whereas the slope for the tapered monolith guide slope has been chosen arbitrarily.

5.2.4 Conclusion: $n - n'$ guide

In this section, a guide system consisting of a tapered monolith guide and a curved guide which loses line of sight of the moderator for all neutrons and still yields a high neutron current at the exit of the curved guide has been developed for the search for sterile neutrons at HIBEAM. Another setup with the elliptic monolith guide and the curved guide was tried out as a possible option, however it is currently not the best one. The curved guide can be further optimized with respect to its dimensions and bending radii, and the monolith guides can be optimized in order to match the curved guide better, to obtain even more cold neutrons at the exit of the curved guide but still lose LOS of the moderator at least once. Furthermore, the problem of background needs to be investigated. For the ANNI design that lost line of sight twice there was still a considerable neutron background 20 m from the source (moderator) [46], implying that the background could be problematic. To summarize, the two setups here explored are both viable options for a guide for $n - n'$ searches at HIBEAM in their current state, but further optimization could be made to maximize the neutron current and minimize the background.

5.3 Comparison $n - \bar{n}$ and $n - n'$ guides

One goal of this project was to compare the different monolith guides tested for the two types of searches at HIBEAM. It is important to remember that it is difficult to define a global figure of merit for multiple experiments, but a discussion and comparison can nevertheless be made.

For the $n - n'$ experiment, both monolith guides have been tested with the curved guide. For $n - \bar{n}$, only the EMG has been tried with two different options for downstream optics. Since a long elliptic guide was the most promising alternative, a similar optimization loop as was done for the EMG in section 5.1.2 was carried out with the tapered monolith guide (see appendix A.2 for details). The result was a maximal FOM of $(2.55 \pm 0.01) \cdot 10^9$ n·s for a length of 25 m and a margin of 0.01 m.

Table 5.16 provides a summary of the guides that have been investigated.

Table 5.16: Comparative table for the EMG and the tapered monolith guide. FOM values are given at the target.

	Elliptic guide	Tapered guide	Ratio EMG/tapered guide
$\boldsymbol{n - \bar{n}}$			
FOM only monolith guide	$1.52 \cdot 10^9$ n·s	$1.09 \cdot 10^9$ n·s	1.40
FOM with second elliptic guide	$3.23 \cdot 10^9$ n·s	$2.55 \cdot 10^9$ n·s	1.26
$\boldsymbol{n - n'}$			
Neutron current at guide exit	$2.22 \cdot 10^{11}$ n/s	$2.48 \cdot 10^{11}$ n/s	0.895

The elliptic monolith guide is clearly better for the $n - \bar{n}$ experiment, even though the effect is lessened when the second elliptic guide is used. With only the tapered monolith guide the focusing is not very efficient so the lower FOM for this one is anticipated, as previously discussed.

For the sterile neutron search, the tapered monolith guide is better. This is also to be expected since this one was better tailored to this experiment. The difference is however less than in the $n - \bar{n}$ case; the loss of using the EMG for $n - n'$ searches is less than the loss of using the tapered guide for $n - \bar{n}$. One could then argue that from this point of view it would be preferable to use the elliptic monolith guide at the HIBEAM beamline.

6 Summary

The main objective, to develop a neutron delivery system for the $n - \bar{n}$ experiment at the HIBEAM beamline, has been satisfied by using an asymmetric elliptic monolith guide together with a second elliptic guide constructed as an extension of the first one. The FOM obtained for this optics setup was $3.2 \cdot 10^9$ n·s, which is higher than the previous FOM for free neutron to antineutron searches obtained at the ILL, even though the flight path for HIBEAM is shorter and the average neutron velocity is higher. An alternative guide concept with a nested mirror system was tried as well, but found to perform worse with the given constraints of the experiment and the current design of the component. In addition, a large elliptic guide is the most reliable option from an engineering point of view. However, the nested mirror component will be an interesting alternative for the NNBAR beamline where the conditions are different, since there will be no guide in the monolith (cf. chapter 2 and [16]).

A guide system for the search for $n - n'$ oscillations was furthermore developed in form of a tapered monolith guide together with a curved guide, satisfying the second objective of this thesis. A comparison was then made between the two monolith guides, which showed that the elliptic monolith guide would seemingly be the overall best option to be used at the HIBEAM beamline.

6.1 Discussion

In the following are some aspects of the simulations performed during the project that are worth discussing.

The exact position of the detector for the HIBEAM experiment is not yet finalized, which means it is not certain that the distance from moderator to detector will be 65 m. The z-positioning has an impact on the FOM value; "the further away the better" roughly speaking, but one must also consider divergence and gravity on very long distances. An increase in distance of P corresponds rougly to an increase in time of flight by the same factor, which would give an increase in FOM of P^2. However, obtaining the best FOM for a $n - \bar{n}$ search is not the ultimate goal of HIBEAM, since NNBAR will obviously be better suited for this. Nevertheless, trying a neutron to antineutron oscillation search already at the HIBEAM beamline at ESS will confirm the feasibility of performing this type of experiment in a spallation facility environment that poses different experimental challenges compared to ILL.

Regarding a further optimization of the $n - \bar{n}$ results, one could for example try other

focusing options and other values for the optical properties. The primary focusing optics used in the project was the ellipse. This is a common choice, but not the only possibility. Parabolic mirrors, which have a different "focusing" effect than elliptic ones, could be tried out to see whether a positive impact on the FOM would be obtained. Furthermore, in most cases the default `McStas` values for the optical properties of the components were used. These could be optimized in a more rigorous manner, for example by including real experimental or manufacturer data, to get a more realistic figure of merit.

6.2 Conclusion

Finally, the results obtained within the scope of this project have shown that a search for $n-\bar{n}$ oscillations could be performed at the HIBEAM beamline at ESS and establish the best current limit for free neutron oscillation searches. This experiment carried out at HIBEAM will also demonstrate the feasibility of the later NNBAR experiment. The high brightness of neutrons at ESS will hence provide great opportunities to study free neutron oscillations. Hopefully this will lead to the observation of a neutron conversion to a sterile and/or antineutron, which in turn would reform the field of particle physics as well as our understanding of the Universe.

Bibliography

[1] *European Spallation Source*, ESS Communications Division. Accessed May 17, 2023. https://europeanspallationsource.se/about.

[2] S. Peggs et al., "ESS Technical Design Report", (2013).

[3] H. Danared, S. Kennedy, and M. Lindroos, "ESS under construction", CERN Courier, https://cerncourier.com/a/ess-under-construction/ (2020).

[4] B. Willis and C. Carlile, *Experimental Neutron Scattering* (Oxford University Press, 2009).

[5] L. Zanini et al., "Design of the cold and thermal neutron moderators for the European Spallation Source", Nuclear Instruments and Methods in Physics Research Section A: Accelerators, Spectrometers, Detectors and Associated Equipment **925**, 33–52 (2019).

[6] A. Addazi et al., "New high-sensitivity searches for neutrons converting into antineutrons and/or sterile neutrons at the European Spallation Source", Journal of Physics G: Nuclear and Particle Physics **48**, 070501 (2021).

[7] V. Santoro, *Search for free Neutron Oscillations at the European Spallation Source: The HIBEAM and the NNBAR program*, May 31, 2022.

[8] G. Kane, *Modern Elementary Particle Physics, Second Edition* (Oxford University Press, 2017).

[9] *The Standard Model*, CERN. Accessed 2023-05-30. https://home.cern/science/physics/standard-model.

[10] R. Foot, "Mirror dark matter: Cosmology, galaxy structure and direct detection", International Journal of Modern Physics A **29**, 1430013 (2014).

[11] A. D. Dolgov, "Baryogenesis, 30 years after", Surveys in High Energy Physics **13**, 83–117 (1998).

[12] *Particle Conservation Laws*, LibreTexts Physics. Accessed 2023-06-14. https://phys.libretexts.org.

[13] HIBEAM/NNBAR Collaboration.

[14] V. Santoro et al., "Development of a High Intensity Neutron Source at the European Spallation Source: The HighNESS project", 10.48550/arXiv.2204.04051 (2022).

[15] F. Backman et al., "The development of the NNBAR experiment", Journal of Instrumentation **17**, P10046 (2022).

[16] R. Wagner et al., "Design of an optimized nested-mirror neutron reflector for a NNBAR experiment", Nuclear Instruments and Methods in Physics Research Section A: Accelerators, Spectrometers, Detectors and Associated Equipment **1051**, 168235 (2023).

[17] *Neutron*, Editors of Encyclopaedia Britannica. Accessed June 14, 2023. https://www.britannica.com/science/neutron, last updated 2023-04-21.

[18] R. L. Workman et al., "Review of Particle Physics", PTEP **2022**, 083C01 (2022).

[19] M. Baldo-Ceolin et al., "A new experimental limit on neutron-antineutron oscillations", Zeitschrift für Physik C Particles and Fields **63**, 409–416 (1994).

[20] K. Abe et al., "Neutron-antineutron oscillation search using a 0.37 megaton-years exposure of Super-Kamiokande", Phys. Rev. D **103**, 012008 (2021).

[21] Y. Kamyshkov in private communication, Feb. 16, 2023.

[22] Z. Berezhiani, "Neutron lifetime puzzle and neutron–mirror neutron oscillation", The European Physical Journal C **79**, 081801 (2019).

[23] Nuclear-power.com, *Neutron energy*, Accessed April 28, 2023. https://www.nuclear-power.com/nuclear-power/reactor-physics/atomic-nuclear-physics/fundamental-particles/neutron/neutron-energy/.

[24] *Neutron optics*, Editors of Encyclopaedia Britannica. Accessed April 28, 2023. https://www.britannica.com/science/neutron-optics, last updated 2018.

[25] A. T. Boothroyd, *Principles of Neutron Scattering from Condensed Matter* (Oxford University Press, 2020) Chap. 9.

[26] R. Wagner, *McStas components for single nested mirror-bank and general- purpose Wolter optic*, Deliverable report D8.1 in project HighNESS – Development of High Intensity Neutron Source at the European Spallation Source. Project Ref. No. 951782. Project website highnessproject.eu, 2021.

[27] T. Chupp, *Neutron Optics and Polarization*, University of Michigan. https://www.ncnr.nist.gov/summerschool/ss09/pdf/Chupp_FP09.pdf.

[28] O. Zimmer, "Imaging nested-mirror assemblies – a new generation of neutron delivery systems?", Journal of Neutron Research **20**, 91–98 (2019).

[29] C. Herb et al., "Nested mirror optics for neutron extraction, transport, and focusing", Nuclear Instruments and Methods in Physics Research Section A: Accelerators, Spectrometers, Detectors and Associated Equipment **1040**, 167154 (2022).

[30] S.-C. Yiu et al., "Status of the Design of an Annihilation Detector to Observe Neutron-Antineutron Conversions at the European Spallation Source", Symmetry **14**, 10.3390/sym14010076 (2022).

[31] E. S. Golubeva et al., "Model of $\overline{n}$ annihilation in experimental searches for $\overline{n}$ transformations", Phys. Rev. D **99**, 035002 (2019).

[32] P. Willendrup and K. Lefmann, "McStas (i): Introduction, use, and basic principles for ray-tracing simulations", Journal of Neutron Research **22**, 1–16 (2020).

[33] P. Willendrup and K. Lefmann, "McStas (ii): An overview of components, their use, and advice for user contributions", Journal of Neutron Research **23**, 7–27 (2021).

[34]P. Willendrup et al., *User and Programmers Guide to the Neutron Ray-Tracing Package McStas, version 3.3* (Physics Department, Technical University of Denmark, 2023), Accessed April 28, 2023. No major changes were made in the updated version, which means the 3.2 version used in the project is still explained well in the version 3.3 manual. https://www.mcstas.org/documentation/manual/mcstas-3.3-manual.pdf.

[35]M. Bertelsen, *McStasScript documentation.* Version 0.0.54 was used in the project (downloaded Jan 23, 2023). https://se.mathworks.com/discovery/monte-carlo-simulation.html.

[36]U. Friman-Gayer and L. Björk, `HIBEAM_McStas`, GitHub repository. https://git.esss.dk/udo.friman-gayer/hibeam_mcstas.

[37]U. Friman-Gayer, `los`, GitHub repository. https://git.esss.dk/udo.friman-gayer/los.

[38]T. Schönfeldt, "Advanced Neutron Moderators for the ESS", DTU Nutech (2016).

[39]J. A. Kulesza et al., *MCNP® Code Version 6.3.0 Theory & User Manual*, tech. rep. LA-UR-22-30006, Rev. 1 (Los Alamos National Laboratory, Los Alamos, NM, USA, Sept. 2022).

[40]Geomview, *Off files*, Accessed May 17, 2023. http://www.geomview.org/docs/html/OFF.html, n.d.

[41]J. Rogers, `Hibeam_mcstas`, GitHub repository. The `Venbla.comp` version used was fetched on 2023-03-24. https://github.com/smjim/HIBEAM_mcstas.

[42]T. Kittelmann et al., "Monte Carlo Particle Lists: MCPL", Computer Physics Communications **218**, 17–42 (2017).

[43]P. M. Bentley, "Instrument suite cost optimisation in a science megaproject", Journal of Physics Communications **4**, 045014 (2020).

[44]J. Rogers in private communication., Mar. 9, 2023.

[45]T. Soldner et al., "ANNI – a pulsed cold neutron beam facility for particle physics at the ess", EPJ Web of Conferences **219**, 10003 (2019).

[46]B. Rataj, "Background Studies of the High-Intensity Baryon Extraction and Measurement (HIBEAM) Experiment at the European Spallation Source", Student Paper. https://lup.lub.lu.se/student-papers/search/publication/9062042 (2021).

A Complementary simulation results

A.1 Velocity and wavelength distributions for EMG and second elliptic guide

The velocity and wavelength spectra in a 1 m diameter annihilation target for the EMG together with the 20 m long second with a 10 mm margin can be found in figure A.1. The average velocity is 1420 m/s and average wavelength 3.27 Å.

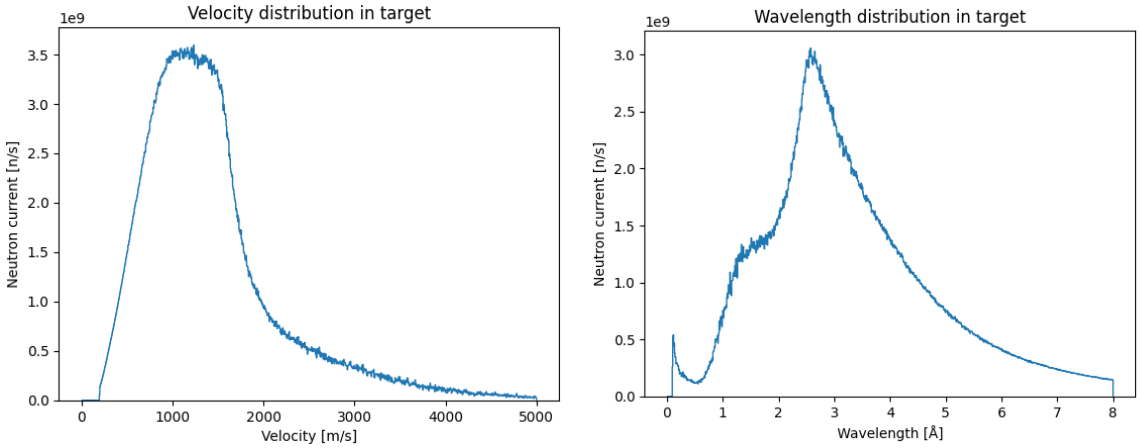

(a) Velocity distribution.

(b) Wavelength distribution.

Figure A.1: Velocity and wavelength distributions for the EMG and second guide with optimal parameters in a 1 m diameter target. The number of tracks for this simulation was 10^8.

A.2 Tapered guide with second elliptic guide

The optimization results are shown in figure A.2 for a target diameter of 1 m. The length optimization was performed first, then the margin.

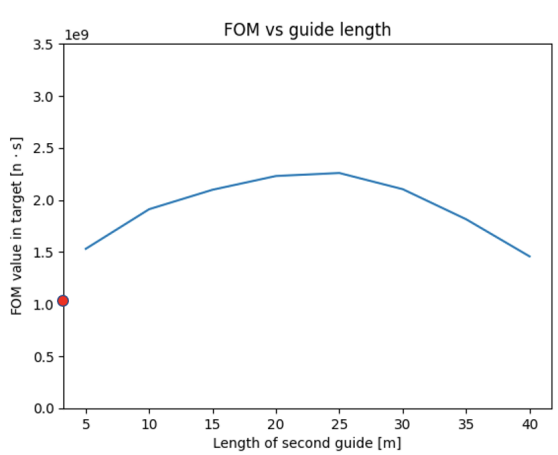

(a) Length optimization. The red dot points out the FOM value without the second guide. Margin is set to 0 m.

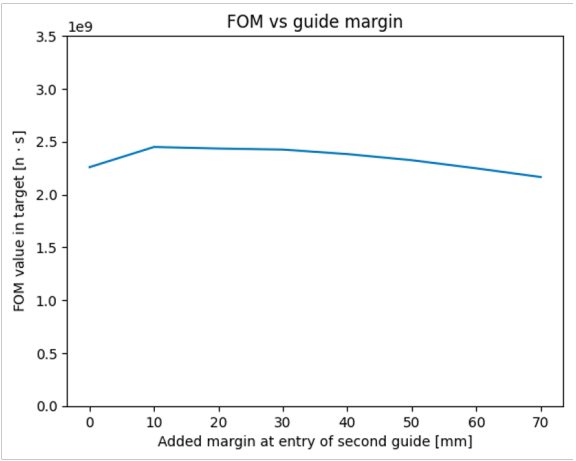

(b) Margin optimization. The length was 25 m.

Figure A.2: Optimization of FOM in a 1 m diameter target for the second elliptic guide.

The optimal parameters were a length of 25 m and a margin of 0.01 m. Results for the setup with the tapered guide and the optimized second elliptic guide are shown in table A.1. The FOM distribution is seen in figure A.3.

Table A.1: Results for the setup with the tapered monolith guide and the second elliptic guide with optimal parameters. The results are compared with the ones for only the tapered guide. The target diameter used is 1 m.

	With second elliptic guide	Only tapered guide
Total neutron current in target [n/s]	$(9.79 \pm 0.07) \cdot 10^{11}$	$(1.28 \pm 0.01) \cdot 10^{12}$
FOM [n·s]	$(2.55 \pm 0.01) \cdot 10^{9}$	$(1.09 \pm 0.01) \cdot 10^{9}$
FOM ratio ILL	1.28	0.543
Optimum target center x [m]	0.0758	0.328
Optimum target center y [m]	-0.0190	-0.285
Average TOF [s]	0.046	0.055

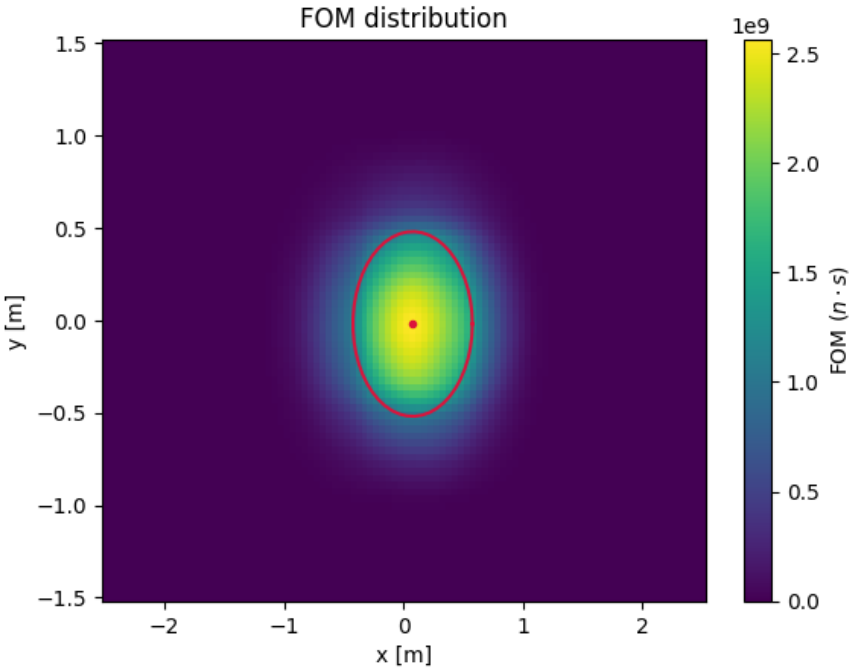

Figure A.3: FOM distribution for tapered monolith guide and the optimized second elliptic guide in a 1 m diameter target.